

DNS-based characterization of pseudo-random roughness in minimal channels

Jiasheng Yang¹, Alexander Stroh¹, Daniel Chung² and Pourya Forooghi^{3†}

¹Institute of Fluid Mechanics, Karlsruhe Institute of Technology, Karlsruhe, Germany

²Department of Mechanical Engineering, University of Melbourne, Victoria 3010, Australia

³Department of Mechanical and Production Engineering, Aarhus University, Aarhus, Denmark

(Received xx; revised xx; accepted xx)

An efficient framework for a systematic study of roughness in a wide roughness parameter space is proposed in the present work. Direct numerical simulation (DNS) is used to study turbulent flow over irregular rough surfaces in the periodic minimal channel configuration. The generation of irregular rough surface is based on a random algorithm, in which the power spectrum (PS) of the roughness height function along with its probability density function (PDF) can be directly prescribed. The hydrodynamic properties of the roughness, particularly the roughness function (ΔU^+) and zero-plane displacement (d), are investigated and compared to those obtained from full-size DNS for 12 roughness topographies with systematically varied PDF and PS and at four roughness heights ($k^+ = 25 - 100$). The comparison confirms the viability of the minimal channel approach for characterization of irregular rough surfaces providing excellent agreement (within 5%) in roughness function and zero-plane displacement across various types of roughness and different regimes. Results also indicates that different random realizations of roughness, with a fixed PS and PDF, translate to similar values of roughness function with a small scatter. The minor uncertainty for the statistical representation of roughness is investigated through the systematic study of the random effect. Based on the results a new perspective of characterizing the roughness using the PDF and PS is proposed. In addition to the global flow properties, the distribution of time-averaged surface force exerted by the roughness onto the fluid is examined and compared to the roughness height distribution for different cases. It is shown that the surface force distribution has an anisotropic structure with spanwise-elongated coherent regions. The anisotropy translates into a very small streamwise integral length scale, which weakly depends on the considered roughness topography, while the larger spanwise integral length scale shows a stronger dependence on roughness characteristics. It is also shown that the sheltering model proposed by Yang *et al.* (2016) describes well the anisotropic spatial distribution of the streamwise surface force. We also studied the coherence function of the roughness height and surface force distributions, and demonstrated that the coherence drops at larger streamwise wavelengths. This can be an indication that structures with very large length-scale are less dominant in contributing to the skin friction. Such a drop in coherence is not observed in the spanwise direction. Finally, multiple existing roughness correlations are assessed using the present roughness dataset. It was shown that the most successful correlations can reproduce the values of equivalent sand-grain

† Email address for correspondence: forooghi@mpe.au.dk

roughness from DNS within $\pm 30\%$ error while none of the correlations shows a superior predictive accuracy.

Key words: Authors should not enter keywords on the manuscript, as these must be chosen by the author during the online submission process and will then be added during the typesetting process (see <http://journals.cambridge.org/data/relatedlink/jfm-keywords.pdf> for the full list)

1. Introduction

Turbulent flows bounded by rough walls are abundant in nature – e.g. fluvial flows (Mazzuoli & Uhlmann 2017), wind flow over vegetation (Finnigan & Shaw 2008) or urban canopies (Coceal & Belcher 2004; Yang *et al.* 2016) – and industry – e.g. degraded gas turbine blades (Bons *et al.* 2001), bio-fouled ship hulls (Hutchins *et al.* 2016), iced surfaces in aero-engines (Velandia & Bansmer 2019) and deposited surfaces inside combustion chambers (Forooghi *et al.* 2018*c*). Systematic study of roughness effects on skin friction dates back to the pioneering works of Nikuradse (1933) and Schlichting (1936). Flow-related roughness can be classified into two types, k-type and d-type roughness. Since the early works by Nikuradse and Schlichting, it has been observed that for a wide range of 3-dimensional industrial roughness, the roughness effect on the flow depends directly on the physical scale of the roughness height k . This type of roughness is thus denoted as k-type roughness. On the other hand, it is widely reported that for some artificially generated regular roughness structures, e.g. smooth surface with a series of closely spaced grooves (Perry *et al.* (1969)), the skin friction coefficient is insensitive to the roughness length scale k , but rather to the outer length scales e.g. the pipe diameter d . Therefore, they are labeled as d-type roughness. The scope of the present work is, however, limited to 3-dimensional irregular rough surfaces, in which k-type behavior is relevant.

For industrial applications the Moody diagram (Moody 1944) has been considered as a standard method to calculate the skin friction of a rough surface. It must be reminded that Moody diagram relates the friction factor to the roughness height ϵ , which is related to a equivalent sand-grain roughness k_s , a quantity that is not known *a priori* for any given irregular rough surface. Hence, for a new roughness topography, estimated k_s needs to be determined using a laboratory or high fidelity numerical experiments or estimated based on a roughness correlations derived from such experiments.

The problem of predicting the roughness-induced friction drag merely based on the knowledge of the roughness topography has received extensive attention in the past, and a variety of roughness correlations have been developed in different industrial contexts (Sigal & Danberg 1990; Waigh & Kind 1998; van Rij *et al.* 2002; Macdonald 2000; Bons 2005; Flack & Schultz 2010; Chan *et al.* 2015; Forooghi *et al.* 2017; Thakkar *et al.* 2017; Flack *et al.* 2020). In these roughness correlations, the topography of the rough surface is often represented by statistical measures of the roughness height map $k(x, z)$, k being the surface height as a function of horizontal coordinates x and z . Some widely discussed statistical measures in this context are summarized by Chung *et al.* (2021), for instance the skewness Sk (Flack & Schultz 2010; Forooghi *et al.* 2017), effective slope ES (Napoli *et al.* 2008; Chan *et al.* 2015), density parameter A_s (Sigal & Danberg 1990; van Rij *et al.* 2002), and correlation length L_x^{corr} (Thakkar *et al.* 2017). Despite extensive work in the past, a universal correlation with the ability to accurately predict the drag of

a generic rough surface remains elusive (Flack 2018). Arguably, development of such a correlation requires a large amount of data from realistic roughness samples. However, generation of such a database has been hindered mainly due to two factors; first, the formidable cost associated with many numerical or laboratory experiments. Second, the relative scarceness of realistic roughness maps and lack of ability to systematically vary their properties. The present work outlines an attempt by the authors to introduce a framework that resolves both issues.

A considerable portion of data in the literature deal with regular roughness - often generated by distribution of similar geometric elements. Examples of studied geometries include cubes (Orlandi & Leonardi 2006; Leonardi & Castro 2010), spheres (Mazzuoli & Uhlmann 2017), pyramids (Schultz & Flack 2009), LEGO bricks (Placidi & Ganapathisubramani 2015), ellipsoidal egg-carton shape (Bhaganagar 2008), and sinusoidal roughness (Chan *et al.* 2015, 2018). In comparison, investigations based on realistic rough surfaces are less frequent and include a much lower number of cases. Notably, Thakkar *et al.* (2017) utilized direct numerical simulation (DNS) to study the effect of roughness topography on flow statistics for 17 industrially relevant irregular surfaces and proposed roughness correlations for transitionally rough regime. Other examples of realistic roughness studies in the framework of wall-bounded turbulence include refs. (Cardillo *et al.* 2013; Yuan & Piomelli 2014; Busse *et al.* 2015, 2017; Forooghi *et al.* 2018c; Yuan & Aghaei Jouybari 2018).

In recent years, mathematically generated irregular roughness has received an increased attention as means to systematically approach a universal roughness correlation. One of the earliest attempts of this kind was made by Scotti (2006) who proposed a method to produce virtual sand roughness by random distribution of ellipsoids. Others adopted randomized roughness generation concepts based on discrete elements (Forooghi *et al.* 2017, 2018a; Kuwata & Kawaguchi 2019), ripples (Chau & Bhaganagar 2012) or superposition of sinusoids (De Marchis *et al.* 2020) to generate irregular roughness. In an attempt to study turbulence over surfaces that closely resemble realistic roughness, Jelly & Busse (2019) generated height maps, $k(x, z)$, using weighted linear combinations of Gaussian-distributed random numbers. In their large eddy simulation (LES) study focused on realistic complex terrain, Anderson & Meneveau (2011) used random Fourier modes to create surfaces with power-law power spectra ($E(q) \propto q^p$ - where q is the wavenumber and p is a constant). Barros *et al.* (2018) employed a modified version of this roughness generation method to study the effect of spectral slope p on the friction drag using turbulent water channel experiments. It must be noted that while the power spectrum (PS) of roughness height determines the distribution of roughness wavelengths (horizontal scales), it does not directly control the probability distribution function (PDF) of the roughness height, which determines common topographical factors, such as k_{rms} and Sk . In this respect, while the majority of the above cited works deal with Gaussian PDFs, naturally occurring roughness can be highly non-Gaussian (Bons *et al.* 2001; Monty *et al.* 2016; Thakkar *et al.* 2017). Indeed many previous studies highlighted significant impact of departure from Gaussian distribution - mainly measured by skewness - on the mean flow and turbulent statistics (Flack & Schultz 2010; Jelly & Busse 2018; Kuwata & Kawaguchi 2019). Motivated by that, recently Flack *et al.* (2020) generated non-Gaussian rough surfaces using the Pearson system random numbers, in which the skewness and kurtosis of the PDF can be prescribed. These mathematically generated surfaces were then tested in a water channel facility to determine the relation between k_s and skewness for realistic roughness. In the present paper, we adopt an alternative roughness generation method (Pérez-Ràfols & Almqvist 2019), which provides the flexibility to prescribe any desired combination of PDF and PS. The algorithm offers more robustness and freedom

(prescribing the full PDF rather than a few moments) compared to the algorithms based on translations of Pearson’s or Johnson’s types (Pérez-Ràfols & Almqvist 2019) and can be utilized for generation of roughness samples that serve as surrogates of realistic roughness in friction drag studies. As we implemented the random roughness generation tool in such a way that the roughness structures are manipulated in a statistical sense, we refer to the roughness samples generated by this method as ‘pseudo-random’ roughness in the present article.

As mentioned above, both experiments and numerical simulations have been employed in the past to study turbulent flows over rough walls. Multiple experiment and simulation campaigns have been conducted in roughened pipes (Nikuradse 1933; Langelandsvik *et al.* 2008; Chan *et al.* 2015), developing boundary layers (Flack *et al.* 2007; Cardillo *et al.* 2013; Barros & Christensen 2019), channels (Flack *et al.* 2016; Napoli *et al.* 2008; Bhaganagar 2008; Orlandi & Leonardi 2006) and open channels (Chan-Braun *et al.* 2011; Forooghi *et al.* 2017). In recent years, DNS has been the pacing approach in studying the effect of roughness topography on friction drag. Standard DNS, however, involves resolving the entire spectrum of turbulent length scales ranging from the large geometrical scales to the small viscous scale, which is computationally costly. For wall-bounded turbulence simulations the cost of DNS scales with Re_τ^3 (Pope 2000), which means that covering a wide roughness topography parameter space by DNS is prohibitively expensive even at moderate Reynolds numbers. To tackle this problem, Chung *et al.* (2015) and MacDonald *et al.* (2016) employed the idea of DNS in minimal span channels (Jiménez & Moin 1991; Flores & Jiménez 2010) for prediction of roughness-induced drag over a regular sinusoidal roughness in a channel. The central idea followed by these authors is that the amount of downward shift in the inner-scaled velocity profile ΔU^+ is the determining factor in the prediction of drag. These authors showed that, thanks to outer layer similarity of wall bounded turbulence (Townsend 1976), this key quantity can be accurately predicted by minimal rough channels. This can be achieved as long as an adequately large range of near-wall structures are accommodated in the simulation domain despite the fact that exclusion of larger outer structures leads to the deterioration of the solution in the outer layer. The same group of authors further developed the idea for channels with minimal streamwise extent (MacDonald *et al.* 2017), high aspect ratio transverse bars (MacDonald *et al.* 2018) and also for passive scalar calculations (MacDonald *et al.* 2019). These efforts established the following criteria for the size of a minimal channel based on simulations with 3D sinusoidal roughness:

$$L_z^+ \geq \max\left(100, \frac{\tilde{k}^+}{0.4}, \lambda_{\text{sin}}^+\right), \quad (1.1)$$

$$L_x^+ \geq \max(1000, 3L_z^+, \lambda_{\text{sin}}^+). \quad (1.2)$$

Here L_z and L_x are the spanwise and streamwise extent of the minimal channel, respectively, λ_{sin} is the sinusoid wavelength of roughness, \tilde{k} is the characteristic roughness height (here sinusoid amplitude) and the plus superscript indicates viscous scaling. Here the main pursue of the guidelines is to adjust the size of minimal channel based on the scales of investigated roughness topography as well as the size of near wall turbulence structures. MacDonald *et al.* (2017) showed that the calculated flow field can be considered as ‘healthy turbulence’ up until a critical height $y_c^+ \approx 0.4L_z^+$.

While the aforementioned efforts showed the potential of minimal channels in determination of roughness-induced drag, a formal extension of this concept to irregular roughness is yet to be made (Aghaei Jouybari *et al.* 2021). One must specifically note that, the sinusoidal roughness topography studied by Chung *et al.* (2015) and MacDonald

et al. (2017, 2019) composes of repetitive patterns meaning that the roughness geometry in a minimal channel is an exact subset of the original surface. For realistic roughness, it is important to understand if the same concept can be applied when the minimal and the original roughness samples are merely similar in a ‘statistical’ sense. Recently, Alves Portela & Sandham (2020) attempted to predict flow over a realistic roughness combining minimal channels with a novel hybrid DNS/URANS model. While their hybrid model generated similar results to the pure DNS in case of channels with the same size, their predicted k_s in minimal channels did not necessary match those in the larger ones due to the fact that their roughness sub-sample failed to preserve full scale roughness properties, as was implied by the deteriorated roughness statistics. This observation further highlights the need for careful investigation of minimal channel concept for realistic roughness. Although some previous researchers, e.g. Aghaei Jouybari *et al.* (2021), have already applied the concept for random surfaces successfully, no systematic verification of minimal channel approach for irregular roughness of random nature has been reported in the past. In the present work, we aim at filling this gap by investigating 12 types of roughness topographies systematically covering a large portion of roughness parameter space. In the present work, we use the flexibility provided by the pseudo-random roughness generation algorithm to systemically study the application of minimal channel concept for irregular roughness. To this end we compare simulations of flow in minimal and full channels with roughness topographies that are ‘statistically’ similar. In doing so, we aim to address three main research questions; what are the generalized rules for the size requirements of the minimal channel for any arbitrary rough surface? What are the statistical properties that can uniquely determine hydrodynamic properties of roughness? And what are the limitations of minimal channel approach when applied to stochastic roughness? To ensure the generalizability of our answers the problem is studied for a wide range of roughness types and also for both transitionally and fully rough regimes. With the proposed framework a systematic study of roughness in a wide roughness parameter space, that have not been considered yet, is carried out with minimum resource consumption. In addition, we also study the local distribution of surface force on the irregular rough surfaces. Through comparison with roughness height distribution, this can shed light on the question of which roughness scales contribute the most to the overall drag force. This can be used in future laboratory and numerical studies where certain scales have to be filtered due to test section or domain size limitations.

The paper is organized in the following way. The methodology of pseudo-random roughness generation will be introduced in section 2.1. Simulation configurations will be described in section 2.2. An overview of the simulation cases is presented in section 2.3. Then the post-processing methodology is discussed in section 2.4. The simulation results are discussed in section 3, in which evaluation of minimal channel concept (section 3.1), correlation of surface force with roughness map (section 3.2), effect of roughness geometry on global parameters (section 3.3) and an assessment of existing correlations (section 3.4) are presented.

2. Numerical methodology

2.1. Pseudo-random roughness generation

As mentioned in the introduction, the roughness generation method proposed by Pérez-Ràfols & Almqvist (2019) is adopted in the present methodology. In this method both wall-parallel and wall-normal statistical properties of the roughness can be adjusted. Here wall-parallel properties refer to the PS of the roughness structures and wall-normal

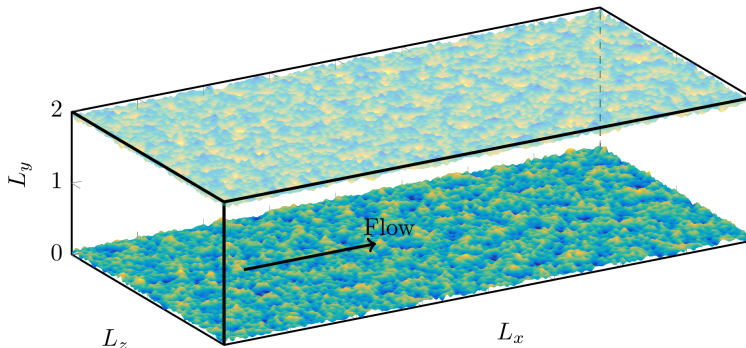


Figure 1: Schematic representation of simulation domain with an example pseudo-realistic surface mounted. Normalization of lengths with H is applied in the figure.

properties refer to the PDF of the surface height. The roughness map is represented by a discrete elevation distribution on a 2-dimensional Cartesian grid. The generation algorithm used in the present work takes the target PDF and PS as inputs. Transformations between the physical space and spectral space is done by discrete fast Fourier transform. Initially a roughness map k_{PDF}^0 is generated which has the prescribed PDF but not necessarily the prescribed PS. This initial map is then corrected in the Fourier space according to the prescribed PS, which is represented by \hat{k}_{PS}^i :

$$\hat{k}_{\text{PS}}^{i+1} = \hat{k}_{\text{PDF}}^i \frac{|\hat{k}_{\text{PS}}^i|}{|\hat{k}_{\text{PDF}}^i|}. \quad (2.1)$$

where i indicates the iteration of the generation process. The output of this stage k_{PS}^{i+1} , has the desired PS but not necessarily the prescribed PDF. In the present notation, subscripts PDF and PS indicate that the roughness field has the desired PDF or PS, respectively. The hat indicates the Fourier transform. After which k_{PDF}^{i+1} is updated by correcting the PDF of k_{PS}^{i+1} by rank ordering. This correction process continues for n iterations until both k_{PDF}^n and k_{PS}^n converge to a height map with the target PDF and PS within a predetermined error. For more details on the the generation algorithm, the readers are referred to reference (Pérez-Ràfols & Almqvist 2019).

2.2. Direct numerical simulation

A number of DNS have been carried out in fully developed turbulent plane channels, in which the flow is driven by a constant pressure gradient. A representation of the simulation domain is shown in figure 1, where x , y and z denote streamwise, wall-normal and spanwise directions with respective velocity components u , v and w . The roughness are mounted on both upper wall and lower wall. Channel half height, which is the distance between the deepest trough in roughness and the centre plane of the channel, is labeled as H and will be used to normalize the geometrical scales. The incompressible Navier-Stokes equations are solved using the pseudo-spectral solver SIMSON (Chevalier *et al.* 2007), where wall-parallel directions are discretized in Fourier space, while in wall-normal direction Chebyshev discretization is employed. Immersed Boundary Method (IBM) based on Goldstein *et al.* (1993) is used to impose the no-slip boundary condition on the roughness by introducing an external volume force field directly to the Navier-Stokes equation. The presently used IBM implementation has been validated and used in previous studies (Forooghi *et al.* 2018b; Vanderwel *et al.* 2019; Stroh *et al.* 2020).

The Navier-Stokes equation writes

$$\nabla \cdot \mathbf{u} = 0, \quad (2.2)$$

$$\frac{\partial \mathbf{u}}{\partial t} + \nabla \cdot (\mathbf{u}\mathbf{u}) = -\frac{1}{\rho} \nabla p + \nu \nabla^2 \mathbf{u} - \frac{1}{\rho} P_x \hat{\mathbf{e}}_x + \mathbf{f}_{\text{IBM}}, \quad (2.3)$$

where $\mathbf{u} = (u, v, w)^\top$ is the velocity vector and P_x is the mean pressure gradient in the flow direction added as a constant and uniform source term to the momentum equation to drive the flow in the channel. Here p , $\hat{\mathbf{e}}_x$, ρ , ν and \mathbf{f}_{IBM} are pressure fluctuation, streamwise basis vector, density, kinematic viscosity and external body force term due to IBM, respectively. Periodic boundary conditions are applied in the streamwise and spanwise directions. No-slip boundary condition is applied on the rough walls. The friction Reynolds number is defined as $\text{Re}_\tau = u_\tau(H - k_{\text{md}})/\nu$, where $u_\tau = \sqrt{\tau_w/\rho}$ and $\tau_w = -P_x \cdot (H - k_{\text{md}})$ are the friction velocity and wall shear stress, respectively. Melt-down height denoted by k_{md} is the mean roughness height measured from the deepest trough. Note that we use $(H - k_{\text{md}})$ which is the mean half cross section area divided by the channel width – or arguably the effective channel half height – as the reference length scale in these definitions. In total, four different values of Re_τ in the range of 250-1000 are simulated in the present work in order to be able to cover different regimes. The simulations designed to study the effect of roughness topography are, however, performed mainly at $\text{Re}_\tau = 500$.

The simulation domain is discretized in equidistant grid in wall-parallel directions while in wall-normal direction cosine stretching based on Chebyshev node distribution is applied. The selection of grid size must take into consideration both flow and roughness length scales. As reflected by Busse *et al.* (2015), each roughness wavelength should be represented by multiple computational cells. Since we prescribe the PS in the roughness generation approach, the range of present roughness wavelengths can be prescribed. Here the smallest roughness wavelength, labeled as λ_1 , is the crucial quantity for horizontal grid resolution. Therefore, in the view of the present computational capacity, $\lambda_1 = 0.08H$ is prescribed for the following simulations. Mesh independence study is carried out, from which the smallest roughness wavelength being resolved by 8-10 cells in each directions is found adequate to obtain the converged double averaged velocity profile. Overall, the grid size $\Delta^+ < 5$ in wall-parallel directions is proven to be appropriate through the mesh independence test. In wall-normal directions, cosine stretching mesh is adopted for the Chebyshev discretization. It is also checked through the mesh independence test that for present types of rough surfaces, a vertical cell number of 401 is sufficient in delivering a converged result at highest $\text{Re}_\tau \approx 1000$, thanks to the overresolving of roughness structure by cosine stretching grid near wall. An exemplary illustration of the grid configuration at $\text{Re}_\tau = 500$ in the near wall region is shown in Appendix A.

2.3. Description of cases

Using the roughness generation algorithm introduced in section 2.1, multiple samples are generated. In the present work, different types of PDF will be combined with power-law PS, that is $E_k(\mathbf{q}) = C_0(\|\mathbf{q}\|/q_0)^p$, where \mathbf{q} is the wavenumber vector $\mathbf{q} = (q_x, q_z)^\top$, $q_0 = 2\pi/\lambda_0$ is the smallest wavenumber corresponding to the largest in-plane length scale λ_0 , C_0 is a constant to scale the roughness height, and p is the spectral slope of the power-law PS. The overview of the configurations of PDF and PS is illustrated in figure 2. In figure 2 (b,c,d) the PS density normalized by the r.m.s. of the roughness height are compared in pairs. The upper and lower cutoff wavelength λ_0 and λ_1 are transformed to cutoff wavenumbers $q_0 = 2\pi/\lambda_0$ and $q_1 = 2\pi/\lambda_1$, which are represented by the red dashed lines in figure 2 (b,c,d) on the left and right side of the figures respectively. As stated

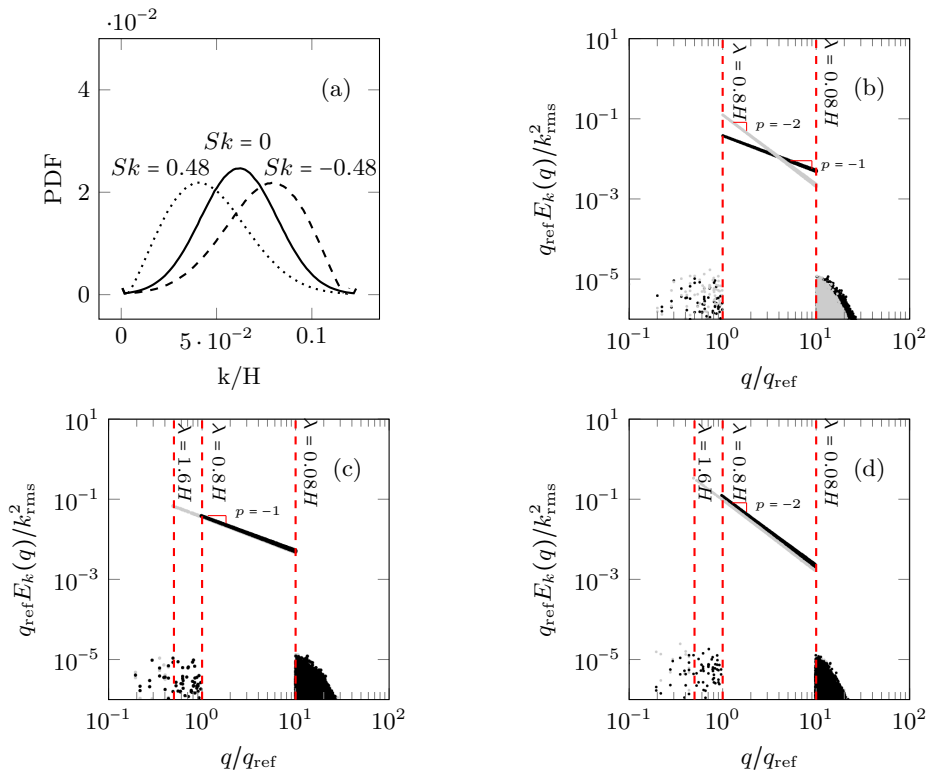


Figure 2: Statistical representation of the studied Roughness. (a): PDF of roughness, (b): Normalized PS density with different p , (c): Normalized PS density with different λ_0 , $p = -1$, (d): Normalized PS density with different λ_0 , $p = -2$. In (b,c,d) wavenumber q is normalized by the reference wavenumber $q_{\text{ref}} = 2\pi/(0.8H)$. Vertical dashed lines are high-pass filtering and low-pass filtering, corresponding to λ_0 & λ_1 respectively.

in the previous section, the lower cutoff wavelength is related to the grid resolution and a value of $\lambda_1 = 0.08H \approx 8\Delta_x \approx 8\Delta_z$ is applied for all roughness topographies in the present work. With an isotropic roughness and a fixed λ_1 , the PS is determined by two remaining parameters, λ_0 and p . In present work, two values of p ($p = -1$ and $p = -2$) are examined, the PS of which are shown in figure 2 (b). For the selection of p values we seek similarity to previous works (Anderson & Meneveau 2011; Barros *et al.* 2018; Nikora *et al.* 2019). Moreover, two different upper cutoff wavelengths ($\lambda_0 = 0.8H$ and $\lambda_0 = 1.6H$) of the roughness PS are investigated. Power spectrum with $\lambda_0 = 0.8H$ and $1.6H$ with identical slopes p are compared in figure 2(c,d), where wavenumber q is normalized by referencing wavenumber $q_{\text{ref}} = 2\pi/(0.8H)$

Three types of PDFs with positive, zero and negative skewness are examined in the present work. Covering a relatively large range of Sk is intended to ensure that the results can be generalized to a wide spectrum of naturally occurring roughness in different applications. The non-skewed roughness is described by a Gaussian distribution. For the positively skewed roughness, Weibull distribution is used, which writes

$$f(k) = K\beta^K k^{(K-1)} e^{-(\beta k)^K}, \quad (2.4)$$

where the parameters K and β can be used to adjust the standard deviation and skewness

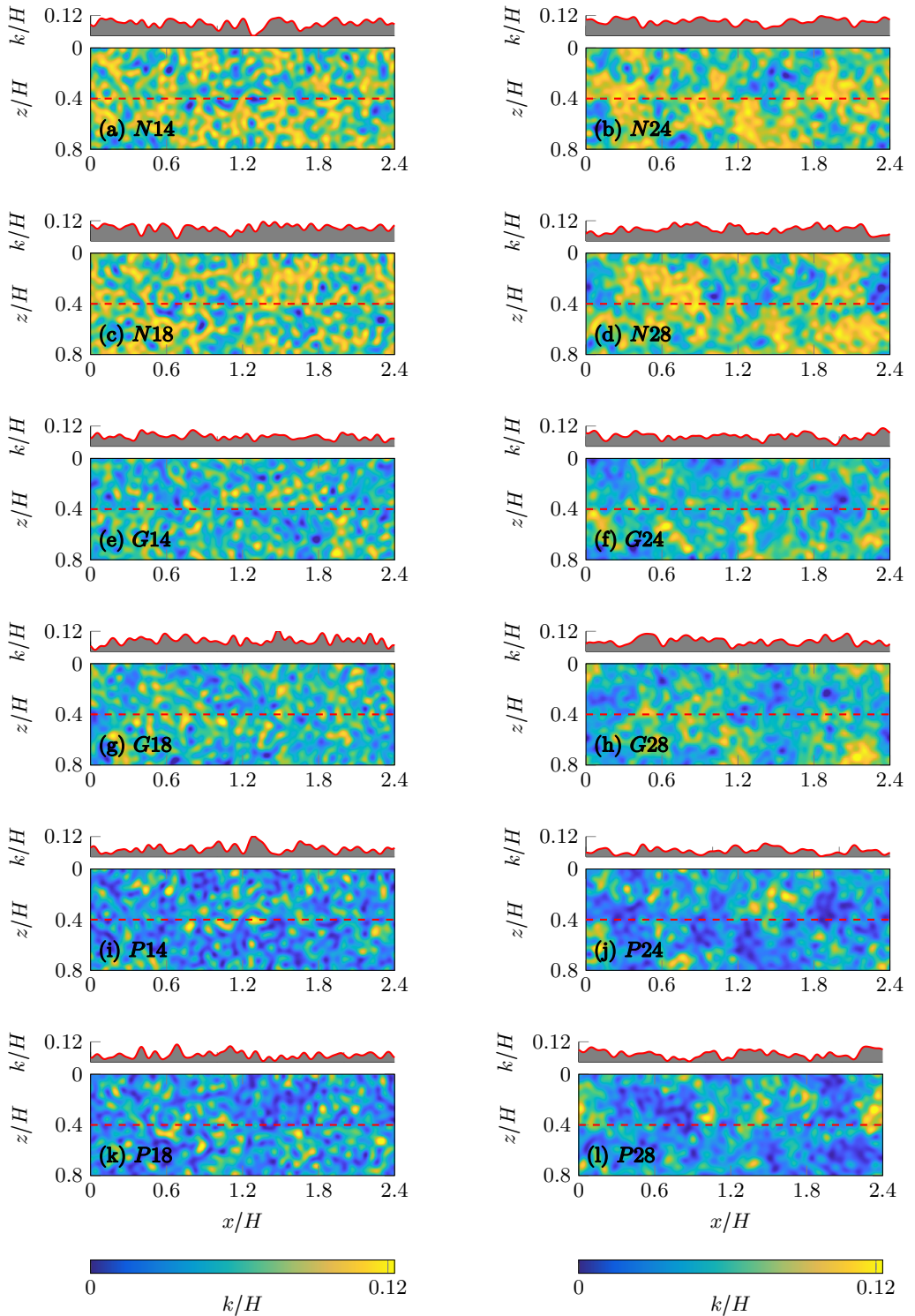


Figure 3: Roughness maps with configuration $M1 - 500$, color indicates height. 1D roughness profile at $z = 0.4H$ (---) is shown above each roughness map. (a-d): negatively skewed, (e-h): zero skewness, (i-l): positively skewed; left column: $p = -1$. right column, $p = -2$.

of the distribution. The skewness is always adjusted to the value of 0.48. Similar to the Gaussian distribution the Kurtosis of the Weibull distribution is always equal to three. A negatively skewed PDF is obtained by flipping the PDF of a positively skewed Weibull PDF. Here $Sk = -0.48$ is prescribed. In the present work, the 99% confidence interval of roughness height PDF, k_{99} , is used as the characteristic size of roughness, i.e. $k = k_{99}$. This measure is related to the standard deviation of the roughness, and hence can be directly prescribed. We used a fixed value of $k = 0.1H$ in all cases. Indeed, k is a statistical measure of maximum peak-to-trough roughness size, which unlike the absolute peak-to-trough size k_t , is not deteriorated by extreme events. These types of PDFs are illustrated in figure 2. Moreover, in order to avoid extreme high roughness elevations in the simulations, roughness heights outside 1.2 times the 99% confidence interval of PDF are excluded. Therefore, the peak-to-trough height $k_t = 0.12H$ is achieved for all roughness in the present work. Combining the three types of PDF (with different values of Sk) with four types of PS (two values of p and λ_0 each) twelve different roughness topographies are studied in the present work, which are summarized in table 1. Selected patches of all 12 roughness topographies on surfaces with size $2.4H \times 0.8H$, are displayed in figure 3. Above each roughness map, the 1D roughness profile at $z = 0.4H$ along streamwise direction is shown.

For each roughness sample, simulations in full-span and minimal channels are carried out. For minimal channels the spanwise size L_z is the main subject of the study. As the log-layer flow structures are set by the spanwise dimension L_z (Flores & Jiménez 2010), it is often most critical in terms of reducing the computational cost. The spanwise size of the present minimal channels are designed to fulfil the three criteria set by inequality (1.1). The first criterion ($L_z^+ > 100$) stems from the fact that the computational domain must accommodate the near wall cycle of turbulence and, unlike the other two criteria, is independent of the roughness topography. The second criterion ($L_z^+ \geq \tilde{k}^+/0.4$) ensures that roughness can be included in 'healthy turbulent' zone under critical height. We translate the criteria for a realistic roughness by replacing \tilde{k} for the sinusoidal roughness by the characteristic roughness height k for any arbitrary roughness. The third criterion states that the minimal channel should contain the roughness wavelength. However, for the realistic surfaces a single characteristic wavelength is not naturally determined. A conservative choice for this limit of the channel width can be the largest in-plane length scale, which is λ_0 in the present study. This ensures that all wavelengths present in the roughness topography are included in the spanwise domain. Recalling the aim of reducing the roughness simulation cost, however, we seek a less conservative choice, in which some of the larger wavelengths are excluded. Particularly, for simulations of engineering roughness, it is often impractical to include extremely large roughness scales. To formalize our choice, we denote the largest spanwise wavelength that a domain can accommodate as λ^* , and calculate the portion of surface energy that larger wavelengths contribute to the original roughness as

$$\Phi_c \left(\frac{2\pi}{\lambda^*} \right) = \frac{\int_{2\pi/\lambda^*}^{2\pi/\lambda_1} E_k(q) dq}{\int_{2\pi/\lambda_0}^{2\pi/\lambda_1} E_k(q) dq}. \quad (2.5)$$

where λ is the discrete wavelength. If the spanwise domain size is λ^* , the simulation resolves a roughness with Φ_c portion of the original surface variance.

In the current research we examine a choice of spanwise channel size corresponding to half the size of the largest length scale, i.e. $\lambda_0/2$. With the adopted power-law PS, it leads to the values of Φ_c equal or larger than 90% for all samples under investigation. Hence the third criterion is replaced by $L_z \geq \lambda_{1/2}$, where $\lambda_{1/2} = \lambda_0/2$, which means that

the simulations resolve at least 90% of the original surface variance. The new criterion leads to a minimum channel width of $L_z = 0.8H$ for half of the investigated roughness topographies (those with $\lambda_0 = 1.6H$) and $L_z = 0.4H$ for the other half (those with $\lambda_0 = 0.8H$). We label the minimal channels with the former (larger) and latter (smaller) spanwise sizes as $M1$ and $M2$, respectively. For roughness samples with $\lambda_0 = 0.8H$ simulations at both $M1$ and $M2$ channels are carried out. To complete the investigation, some simulation with a further reduced channel size $M3$ ($L_z = 0.3H$) are carried out. It is worth mentioning that, since $k = 0.1H$ holds for all topographies, $M1$, $M2$ and $M3$ channels fulfill the $L_z \geq k/0.4$ criterion. For all simulation configurations the streamwise channel size L_x is set according to the equation 1.2 once L_z is known.

Simulations are carried out at four different friction Reynolds numbers $Re_\tau = 250, 500, 750$ and 1000 , at fixed $k/H = 0.1$, leading to $k^+ = 25, 50, 75$, and 100 . However the parametric study on roughness topography is only conducted at $k^+ = 50$. Apart from minimal channel simulations, conventional full span channel simulations with the size $L_x \times L_y \times L_z = 8H \times 2H \times 4H$, labeled as F , are also carried out for all roughness topographies. For the two highest Reynolds numbers, however, such large simulations are costly. Consequently, for these Reynolds numbers, the largest investigated channels are smaller than the F channel (but still larger than $M1/M2/M3$). These channels are labeled as $M0$. Table 2 summarizes the details of all simulations carried out for rough channels. In order to provide a reference for determining the roughness function ΔU^+ , additional smooth-wall simulations are also performed in $M2$, $M1$ and F -sized channels at $Re_\tau = 500$ (not shown in the table). Overall, each rough-wall simulation case is defined by a combination of roughness topography and simulation configuration (channel size and Reynolds number). Throughout the article, the following naming convention is used to describe the cases:

$$\begin{array}{c}
 \text{Topography} \\
 \hline
 \boxed{G} \quad \boxed{2} \quad \boxed{4} \\
 \hline
 \text{PDF} \quad -p \quad 10\lambda_{1/2}/H \\
 \hline
 \text{Simulation configuration} \\
 \hline
 \boxed{F} - \boxed{500} \\
 \hline
 \text{ch. size} \quad 10k^+
 \end{array} . \quad (2.6)$$

- The first character indicates the type of PDF; G for Gaussian distribution, P for positively skewed ($Sk \approx 0.48$), and N for negatively skewed ($Sk \approx -0.48$).
- The second digit indicates the PS spectral slope; 1 for $p = -1$ and 2 for $p = -2$.
- The third digit represents the half of large cutoff wavelength $\lambda_{1/2}$, with which channel width is determined; 4 for $\lambda_{1/2} = 0.4H$ and 8 for $\lambda_{1/2} = 0.8H$.
- The following character(s) indicates the channel spanwise size; F for full channel ($L_z = 4H$), $M1$ and $M2$ for the larger ($L_z = 0.8H$) and the smaller ($L_z = 0.4H$) minimal channels, respectively. $M3$ utilizes the spanwise width $L_z = 0.3H$. $M0$ is introduced to the cases which $k^+ = 75$ and 100 with $L_z = 2H$ and $1H$, respectively
- The last number denotes $10k^+$, or equivalently, Re_τ .

2.4. Post-processing

The time-averaged flow field over a rough surface is heterogeneous in horizontal directions. In order to analyze the one-dimensional mean profile of the flow, we apply double averaging, as proposed by Finnigan & Shaw (2008). The double-averaged velocity profile in the wall-normal direction $\langle \bar{u} \rangle(y)$ is obtained by averaging the time-averaged velocity over wall-parallel directions, i.e.

$$\langle \bar{u} \rangle(y) = \frac{1}{S} \iint_S \bar{u}(x, y, z) dx dz . \quad (2.7)$$

Topography	Sk	p	λ_0/H	k_a/H	k_{md}/H	k_{rms}/H	L_x^{corr}/H	S_f/S	ES_x
P14	0.48	-1	0.8	0.017	0.046	0.0208	0.050	0.28	0.57
P18	0.48	-1	1.6	0.017	0.046	0.0208	0.054	0.27	0.54
P24	0.48	-2	0.8	0.017	0.046	0.0208	0.104	0.21	0.44
P28	0.48	-2	1.6	0.017	0.046	0.0208	0.170	0.19	0.39
G14	0	-1	0.8	0.016	0.061	0.0200	0.050	0.27	0.54
G18	0	-1	1.6	0.016	0.061	0.0200	0.054	0.26	0.53
G24	0	-2	0.8	0.016	0.061	0.0200	0.104	0.20	0.43
G28	0	-2	1.6	0.016	0.061	0.0200	0.168	0.18	0.37
N14	-0.48	-1	0.8	0.017	0.074	0.0208	0.050	0.28	0.57
N18	-0.48	-1	1.6	0.017	0.074	0.0208	0.054	0.27	0.54
N24	-0.48	-2	0.8	0.017	0.074	0.0208	0.104	0.21	0.44
N28	-0.48	-2	1.6	0.017	0.074	0.0208	0.170	0.19	0.39

Table 1: Roughness topographical properties, where $Sk = (1/k_{\text{rms}}^3) \int_S (k - k_{\text{md}})^3 dS$, $k_a = (1/S) \int_S |k - k_{\text{md}}| dS$ is the mean absolute height deviation from the melt-down height $k_{\text{md}} = (1/S) \int_S k dS$ measured from deepest trough. $k_{\text{rms}} = \sqrt{(1/S) \int_S (k - k_{\text{md}})^2 dS}$ is the standard deviation of the height function. S_f is the total frontal projected area of the roughness. L_x^{corr} refers to the length scale where the roughness auto-correlation in streamwise direction drops under 0.2. $ES = (1/S) \int_S |\partial k / \partial x| dS$ represents the effective slope.

Topographies	Configuration	Re_τ	L_x/H	L_z/H	N_x	N_z	Δ_x^+	Δ_z^+	$\Delta_{y,k}^+$	FTT
G24	M2 - 250	250	4.0	0.4	512	48	1.95	2.08	0.88	1200
G24	M1 - 250	250	5.0	0.8	576	96	2.17	2.08	0.88	300
G24	F - 250	250	8.0	4.0	900	480	2.22	2.08	0.88	100
G24	M3 - 500	500	2.0	0.3	256	48	3.91	3.13	1.74	1000
* * 4 & G28	M2 - 500	500	2.0	0.4	256	48	3.91	4.17	1.74	2000
all	M1 - 500	500	2.4	0.8	256	96	4.69	4.17	1.74	500
all	F - 500	500	8.0	4.0	900	480	4.44	4.17	1.74	80
G24	M2 - 750	750	1.4	0.4	288	96	3.65	3.13	2.59	1200
G24	M1 - 750	750	2.4	0.8	480	160	3.75	3.75	2.59	300
G24	M0 - 750	750	4.0	2.0	640	320	4.69	4.69	2.59	100
G24	M2 - 1000	1000	1.2	0.4	288	96	4.17	4.17	3.53	500
G24	M1 - 1000	1000	2.4	0.8	576	192	4.17	4.17	3.53	300
G24	M0 - 1000	1000	3.0	1.0	720	240	4.17	4.17	3.53	100

Table 2: Summary of all simulation cases including roughness topography and simulation configurations. For all cases $L_y/H = 2, N_y = 401$. Moreover, * * 4 indicates all roughness topographies with $\lambda_{1/2} = 0.4H$, $\Delta_{y,k}^+$ indicates the grid size at the roughness height i.e. $y = 0.1H$, flow through time (FTT = TU_b/L_x) for statistics collection duration are shown in the last column, where T is the total integral time, $U_b = (1/H_{\text{eff}}) \int_0^H U dy$ is the bulk velocity, $H_{\text{eff}} = H - k_{\text{md}}$.

where $\bar{u}(x, y, z)$ is time averaged streamwise velocity, S is the wall-normal projected plan area (i.e. area of the corresponding smooth wall) and angular bracket $\langle \cdot \rangle$ denotes horizontal averaging. The double-averaged velocity profile $\langle \bar{u} \rangle(y)$ will be denoted as U for simplicity. The time-averaged velocity field is obtained over a long enough period of time.

It is reported by Flores & Jiménez (2010) in their study of smooth minimal channel that, due to the bursting events, simulation time required to achieve converged flow statistics is longer than conventional full span simulation. In order to achieve converged mean velocity profile, a minimum flow-through-time (FTT) is chosen to be 300 for minimal channels. The mean velocity profiles are proven converged for all the cases with 300 FTTs in Appendix B. Initial transients are removed from the statistical integration.

The influence of roughness on the mean flow can be accounted for by a modified coefficient of viscosity ν_e beyond the region where the shape of velocity profile is affected by roughness, i.e. outer layer (Perry & Joubert 1963). This ν_e can be interpreted as a downward shift in logarithmic layer in the inner-scaled streamwise velocity profile relative to the smooth case. This downward velocity shift in the logarithmic region is referred to as roughness function ΔU^+ (Clauser 1956; Hama *et al.* 1954), which is further confirmed by a number of roughness studies, e.g. (Schultz & Flack 2009). In other words, as a result of the outer layer similarity (Townsend 1976), which states that outer-layer flow is unaffected by the near wall events except for the effect due to the wall shear stress, the downward shift of the velocity profile is approximately a constant value in the logarithmic region and possibly beyond if the outer-flow geometry and Reynolds number are matched. Introducing the roughness function to the logarithmic law of the wall (log-law hereafter), it writes

$$U^+ = \frac{1}{\kappa} \ln(y^+ - d^+) + B - \Delta U^+ . \quad (2.8)$$

where $\kappa \approx 0.4$ is the von Kármán constant, $B \approx 5.2$ is the log-law intercept for the smooth wall, d indicates the zero plane displacement which will be talked in detail in the following section, and the superscript $+$ indicates scaling in wall units. Based on the pioneering work by Nikuradse (1933), the roughness function in the fully rough regime is a sole function of the inner-scaled roughness size k_s^+ for the sand-grain roughness according to

$$\Delta U^+ = B - 8.48 + \frac{1}{\kappa} \ln(k_s^+) . \quad (2.9)$$

Equation 2.9 is the basis for the definition of ‘equivalent’ sand-grain roughness (also denoted by k_s) for an arbitrary roughness with the same roughness function.

In the present work, the roughness function ΔU^+ is calculated as the mean offset of the inner-scaled mean velocity profile over the logarithmic layer for the cases with $\text{Re}_\tau \approx 500$. Since corresponding smooth channels in $M2$, $M1$ and F with matched $\text{Re}_\tau \approx 500$ are available, this quantity is calculated by direct comparison to the smooth case. For those cases with varied Re_τ , further smooth channel simulations with matched Re_τ are required in order to derive the corresponding profile shift, which causes unfavourable computational effort. Having in mind that log-law applies for minimal smooth channels under critical height y_c , a good approximation of velocity profile in log region of the smooth channels can be drawn from the log-law, thus ΔU^+ is estimated by the velocity shift at the critical height $y_c^+ = 0.4 \times L_z^+$ relative to the log-law $U^+ = (1/\kappa) \ln(y^+) + 5.2$, where $\kappa = 0.4$.

Finally it must be noted that, unlike a smooth channel, the origin of the wall-normal coordinate for the log-law is not naturally defined for a rough wall. In this regard, Jackson (1981) suggested use of moment centroid of the drag profile on rough surface as the virtual origin for the logarithmic velocity profile. The definition of the virtual wall zero-plane displacement d in present work follows Jackson’s method. The mathematical definition of d following Jackson’s method is given in Appendix C.

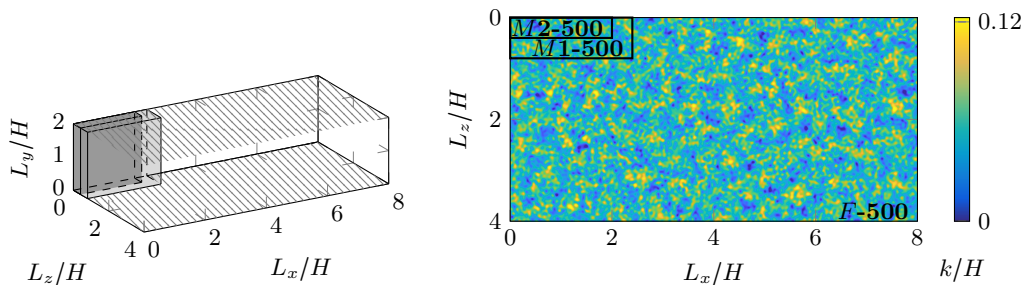


Figure 4: Comparison of channel sizes. Right: Schematic simulation domain of $F - 500$, $M1 - 500$ and $M2 - 500$, hatch pattern represents roughness. Left: Roughness map of $G24F - 500$, black frames indicate minimal channels $M1 - 500$ & $M2 - 500$

3. Results

3.1. Evaluation of minimal-channel simulations

In order to assess the applicability of the minimal channel, the simulations of the roughness topography $G24$ with variation of channel size and k^+ are analyzed. The comparison of different channel sizes at matched $k^+ \approx 50$, i.e. the cases $G24M3 - 500$, $G24M2 - 500$, $G24M1 - 500$ and $G24F - 500$, is discussed in section 3.1.1. This is followed by the results for all different roughness topographies in section 3.1.2. As mentioned before, the roughness generation process in the present research has a random nature, and only statistical properties can be prescribed. To assess the effect of this randomness eight independent simulations are carried out for eight random realizations of the roughness topography $G24$ with $k^+ \approx 50$. The results are presented in section 3.1.3. Finally in section 3.1.4, one roughness topography is studied in a wide range of roughness Reynolds numbers ($k^+ = 25 - 100$) in order to assess the prediction of the minimal channel in different rough regimes. Here the roughness topography $G24$ is evaluated using minimal channels $M2$ and $M1$ and (pseudo) full-span channels $F/M0$.

3.1.1. Minimal channels with different spanwise sizes

The 3D schematic representations of minimal channels $M2$ and $M1$ as well as the full span channel F used for simulations at $k^+ \approx 50$ are shown in figure 4(a); $M3$ is not shown for simplicity. The hatched pattern indicates where the roughness is mounted. Roughness topography $G24$ in the full-size simulation is shown in figure 4(b). For a direct comparison, boundaries of minimal channels $M1$ and $M2$ are represented by the black frames. The pseudo-random surfaces for each configuration is generated independently. That is, for a specific topography, the surface height map in each simulation is unique, but they all share identical statistical properties.

The inner-scaled velocity profiles obtained from roughness topography configuration $G24$ with $k^+ \approx 50$ are shown in figure 5(a). Colored dashed lines are the velocity profiles extracted from smooth channel. The color indicates the size of channel. The critical heights of minimal channels $M2 - 500$ and $M1 - 500$, i.e. $y_c^+ = 0.4 \times L_z^+ = 80$ and 160 are illustrated by black vertical dashed lines in the figure, respectively. While the critical height of $M3 - 500$ i.e. $y_c^+ = 60$ is shown with gray vertical dashed line. It can be observed from the figure, that minimal channel cases $M2 - 500$ and $M1 - 500$ successfully reproduce the velocity profile of a conventional full-span channel under the critical height y_c . The velocity profiles deviate above the critical height y_c due to the nature of minimal

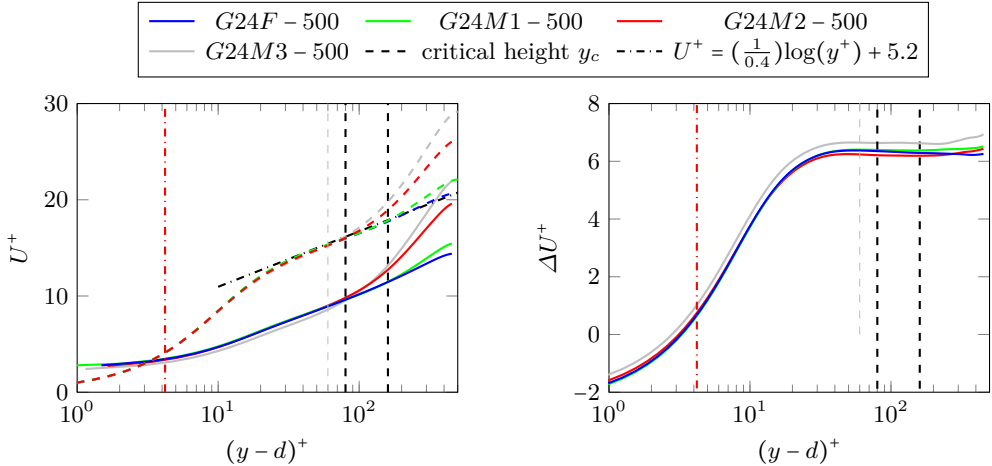


Figure 5: Simulation results of roughness type $G24$. Left: mean velocity profiles (—: Rough, - - -: Smooth), right: velocity offset profiles. Red vertical line indicates roughness height measures from the zero-plane displacement $(k-d)^+$.

channels. For $G24M3-500$, however, some discrepancy of the profile can be observed even under its critical height. In figure 5(b), the velocity offset profiles for F , $M1$ and $M2$ channels are displayed. The velocity offset profiles are obtained by subtracting the rough channel velocity profile from each corresponding smooth channel velocity profiles. The velocity offset profile from minimal channels $M1$, $M2$ and full-span channel on the right panel show excellent agreement. Consequently, it seems like the velocity offset is not meaningfully affected by absence of the large wavelengths in spanwise direction with small contribution to the roughness height power spectrum. This however does not hold for channel $M3$ where $\Phi_c(2\pi/L_z) = 82\%$. A similar parameter study performed for roughness topography $G28$ (not shown here) revealed that the velocity offset starts to deviate for channel $M2$ ($\Phi_c(2\pi/L_z) = 84\%$). In both cases the deviation of the velocity profiles starts when the contribution of excluded large wavelengths in the roughness height spectrum is larger than 10%.

It is observed that due to the outer layer similarity the velocity offset in logarithmic layer reaches approximately a constant value. In the present work, ΔU^+ of minimal channels is obtained by averaging the mean velocity offset from each critical height y_c^+ to the half of channel half-height $0.5H^+$, while full span channels is averaged in the region $y^+ = 80 - 250$. This gives $\Delta U^+ = 6.3$ for case $G24F-500$ and $\Delta U^+ = 6.4$ and 6.2 for cases $G24M1-500$ and $G24M2-500$, respectively.

3.1.2. Minimal channels for different roughness topographies

Applying the same analysis to all topographies at $k^+ \approx 50$, roughness function ΔU^+ are calculated and listed in table 3. It has to be mentioned that for case $G24M2-500$, multiple simulations are carried out for the purpose that will be discussed in section 3.1.3. Therefore, roughness function of $G24M2-500$ is the mean roughness function $\overline{\Delta U^+}$ over $G24M2-500$ s and marked with *. The value of ΔU^+ predicted by minimal channels are compared with the prediction by full-span channels with matched topographical property in figure 6. In this plot, the $\pm 5\%$ disagreement interval is illustrated by the green shadow around $\Delta U_{\text{Mini}}^+ / \Delta U_{\text{Full}}^+ = 1$ (red line). Another key quantity widely discussed in the framework of roughness studies is the zero-plane displacement d . Similar to ΔU^+ , d is

Case	ΔU^+			d/k		
	$F - 500$	$M1 - 500$	$M2 - 500$	$F - 500$	$M1 - 500$	$M2 - 500$
$P14$	7.33	7.28	7.35	0.81	0.81	0.82
$P24$	6.99	6.86	6.92	0.78	0.77	0.80
$P18$	7.23	7.34	-	0.81	0.81	-
$P28$	6.57	6.87	-	0.76	0.76	-
$G14$	6.67	6.66	6.56	0.95	0.94	0.95
$G24$	6.30	6.39	6.43*	0.92	0.90	0.92*
$G18$	6.56	6.59	-	0.95	0.95	-
$G28$	5.94	5.88	-	0.90	0.90	-
$N14$	6.14	6.07	5.87	1.06	1.06	1.06
$N24$	5.82	5.63	5.80	1.03	1.03	1.05
$N18$	6.09	6.06	-	1.06	1.06	-
$N28$	5.51	5.58	-	1.01	1.02	-

Table 3: Summary of roughness function ΔU^+ (left) and zero plane displacement d/k (right) at $k^+ \approx 50$, bold values are taken as the minimal channel results. *: mean value over 8 independent $G24M2 - 500$ s

often used as input to roughness models, and therefore, its prediction is of practical value. Motivated by that, in this section we also discuss predictions of d by minimal channels. The value of d/k are also exhibited in the Table 3. Predicted zero-plane displacements d in minimal channels are compared with full span channels in figure 7. It can be observed that minimal channel predictions show excellent agreement with conventional full span channel, the discrepancy lies under 5%. Consistent predictions of roughness function ΔU^+ indicate the capability of the minimal channels in reproducing roughness function ΔU^+ of the irregular pseudo-realistic roughness.

In minimal channel simulations, large turbulent structures in the outer layer cannot be resolved; therefore an unphysical wake behaviour is observed in the outer layer of minimal channels mean velocity profile (see figure 5). However, as the present results suggest, capturing the near wall turbulence in the minimal channel is adequate for the prediction of roughness function ΔU^+ as a quantification of skin friction drag. This, obviously, cannot be generalized to all aspects of the turbulent flow.

3.1.3. Effect of randomness

In the present work, roughness is generated following a pseudo-random process with prescribed PDF and PS. As a result, individually generated rough surfaces with identical statistics are not deterministically identical. This randomness can be a source of uncertainty when pseudo-random roughness is used as a surrogate of realistic roughness. As already observed in figure 6, the estimations of ΔU^+ in minimal channel show some scatter, which indicates a small uncertainty. The pseudo-random roughness generation process can also be considered an imitation of random roughness formation processes in the nature or industry. Hence the results can shed light on the uncertainty introduced by randomness when statistical models are used to predict drag on realistic roughness. To this end, eight rough surfaces corresponding to the identical topographical configuration $G24$ are generated independently. As a consequence, the roughness realization of each randomly generated surface is unique while the statistical properties are nearly identical. To assess the effect of this randomness eight independent simulations are run for eight random realizations of the roughness topography $G24$ with $k^+ \approx 50$ in minimal channel

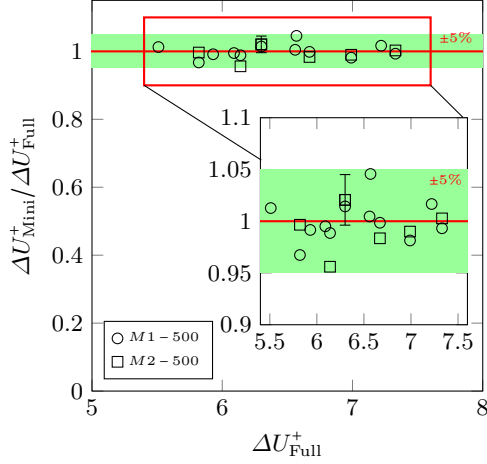


Figure 6: Roughness function predicted by minimal channels ΔU_{Mini}^+ normalized with full span channel prediction ΔU_{Full}^+ , \circ : $M1 - 500$, \square : $M2 - 500$. Green shadow indicates prediction error interval of $\pm 5\%$ around $\Delta U_{\text{Mini}}^+ / \Delta U_{\text{Full}}^+ = 1$ (—). 99% confidence interval is shown for case $G24M2 - 500$

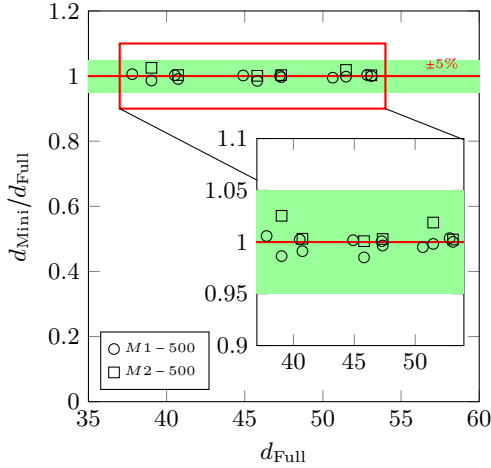


Figure 7: Zero plane displacement predicted by minimal channels d_{Mini}^+ normalized with full span channel prediction d_{Full}^+ , \circ : $M1 - 500$, \square : $M2 - 500$,

$M2$. The computed values of ΔU^+ for all surfaces along with the zero-plane displacement d/k are summarized in table 4. The averaged value of roughness function over the eight $G24M2 - 500$ s is $\Delta U_{G24M2-500}^+ = 6.43$, while the 99% uncertainty interval of all values is 0.31. The averaged ΔU^+ is shown in figure 6 along with the 99% uncertainty interval. One can observe that the uncertainty bar well encompasses the ΔU^+ in the full channel. This can be taken as an indication that minimal channel prediction can approximately converge to the exact value if the main uncertainty due to randomness is ruled out. Nevertheless, as stated before, the error associated with one random realization is still considerably low. Additionally, one cannot rule out a minor influence due to other factors, e.g. the nature of turbulence in the minimal channel, but the present data suggest those influences to be minor if present. It is observed in figure 6 that the 99% confidence bar

Case	ΔU^+	d/k	Case	ΔU^+	d/k
No.1	6.46	0.92	No.5	6.64	0.92
No.2	6.44	0.91	No.6	6.23	0.92
No.3	6.59	0.91	No.7	6.58	0.92
No.4	6.20	0.92	No.8	6.30	0.91

Table 4: Roughness function and zero-plane displacement of $G24M2 - 500s$. Mean roughness function $\Delta U^+_{G24M2-500s} = 6.43$ comparing with $\Delta U^+_{G24F-500} = 6.30$.

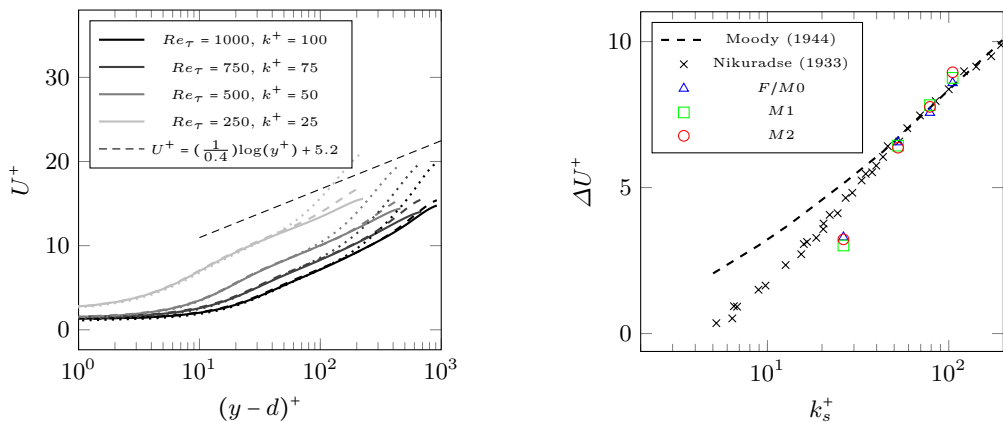


Figure 8: Simulations at different k^+ at fixed k/H ; $k^+ = 25 - 100$. Left: Mean velocity profiles, line color gradually changes from gray to black with increasing Re_τ . (—: $F/M0$, ---: $M1$,: $M2$). Right: Roughness function. Data from Nikuradse’s uniform sand grain roughness and Colebrook relation provide for industrial pipes are added for comparison.

lies in the green area, which is the 5% disagreement. Overall, it can be stated that DNS in minimal channels with matched roughness statistics is an accurate tool for the prediction of ΔU^+ of realistic roughness, apart from the small discrepancy, which is arguably linked to the effect of randomness.

The effect of randomness on the scatter of roughness function can be explained by the fact that PDF and PS are effectively ‘reduced order’ representations of the actual roughness geometry. Even though the results suggest the robustness of this reduced representation for the type of roughness under investigation, a minor difference in ΔU^+ among roughness with the same PDF and PS cannot be ruled out. In other words, while the structure of generated roughness is controlled in a global sense by PDF and PS, the local distribution of roughness features can be varied by the random roughness generation process. For example, occurrence of clustered or streamwise aligned roughness peaks can lead to attenuation of drag due to the sheltering effect, which will be discussed in section 3.2

3.1.4. Minimal channels in transitionally and fully rough regimes

The values of ΔU^+ reported for the simulations with $k^+ \approx 50$ suggest that the flow likely lies in the border between transitionally and fully rough regimes. In order to ensure that minimal channels deliver acceptable predictions in a wide range of scenarios including

both regimes, in this section we study one roughness topography ($G24$) in a range of roughness Reynolds numbers $k^+ \approx 25 - 100$. Both minimal channel simulations $M2$ and $M1$ as well as large-span channel simulations $F/M0$ are carried out. Simulation setups are summarized in table 2. Mean velocity profiles are shown in figure 8(a), while roughness functions ΔU^+ against k_s^+ are shown in figure 8(b). In figure 8(a) the value obtained in minimal channels $M2$ are plotted with dotted lines, $M1$ are plotted with dashed line while (pseudo) full span channels $F/M0$ are represented by solid lines. One can observe from figure 8(a) that each velocity profile deviates above the respective critical height $y_c^+ = 0.4 \times L_z^+$ which are not shown for clarity. However outer-layer similarity can be observed valid from the parallel velocity profile in the outer region. Here roughness functions are obtained by calculating the velocity difference at each critical height relative to the log-law $U^+ = (1/0.4)\log(y^+) + 5.2$. The calculated values of roughness function are shown in figure 8(b) as a function of equivalent sand-grain size k_s^+ . Notably, the calculated values of roughness function from both minimal and full channels show an excellent agreement. Equivalent sand-grain roughness k_s is calculated by fitting roughness function to the asymptotic roughness function in fully rough regime as shown in figure 8(b). In doing so we obtain an equivalent sand-grain roughness size of $k_s \approx 1.05k$ for roughness topography $G24$. The inner-scaled equivalent roughness height k_s^+ on x-axis in figure 8(b) is obtained by scaling the calculated k_s with viscous length scale δ_ν at different Re_τ . It can be observed that ΔU^+ asymptotically approaches fully rough regime at $\Delta U^+ \approx 6$. It is worth mentioning that each data point from figure 8(b) represents unique realization of rough surface. Therefore, it is demonstrated that with identical roughness PDF and PS, hydrodynamic properties of roughness can be uniquely determined. Given the considerable scatter of the roughness function predictions of the roughness with identical statistics from table 1 and 3, a new perspective of more accurately characterizing the roughness using the roughness PDF and PS is thus proposed.

3.2. Roughness surface force

In the present simulations, IBM introduces a volume force within the solid area imposing zero velocity and hence represents the action of pressure and viscous drag force. One of the advantages of IBM is the explicit representation of localized hydrodynamic force exerted by roughness (Chan-Braun *et al.* 2011), here referred to as ‘surface force’. In this section, we investigate the link between the mean surface force distribution and the roughness height distribution. Given the satisfactory performance of the minimal channel demonstrated in section 3.1, the following analysis is carried out based on the results achieved from minimal channels. Previous studies on irregular roughness report that a certain range of roughness scales is dominant in generation of skin friction (Barros *et al.* 2018). A deeper insight into the contribution of different roughness scales to the drag force is the aim of this section. To this end, the local forcing map $\mathbf{f}(x, z)$ is obtained by time-averaging the IBM force field $\mathbf{f}_{\text{IBM}}(x, y, z, t)$ and integrating the force in wall-normal direction y :

$$\mathbf{f}(x, z) = \frac{1}{T} \int_0^H \int_0^T \mathbf{f}_{\text{IBM}}(x, y, z, t) dt dy, \quad (3.1)$$

where $\mathbf{f}(x, z) = (f_x, f_y, f_z)^\top$ is the force vector and f_x , f_y and f_z are streamwise, wall-normal and spanwise force component, respectively. One should note that, precisely speaking, \mathbf{f} equals force per unit density and wall-projected area. Nevertheless, as we are interested in its trend rather than its absolute value, this quantity always appears in a normalized form; hence, for brevity we refer to it as ‘force’. The visualization of normalized forcing map for all $M2 - 500$ cases with their roughness distribution maps are shown in

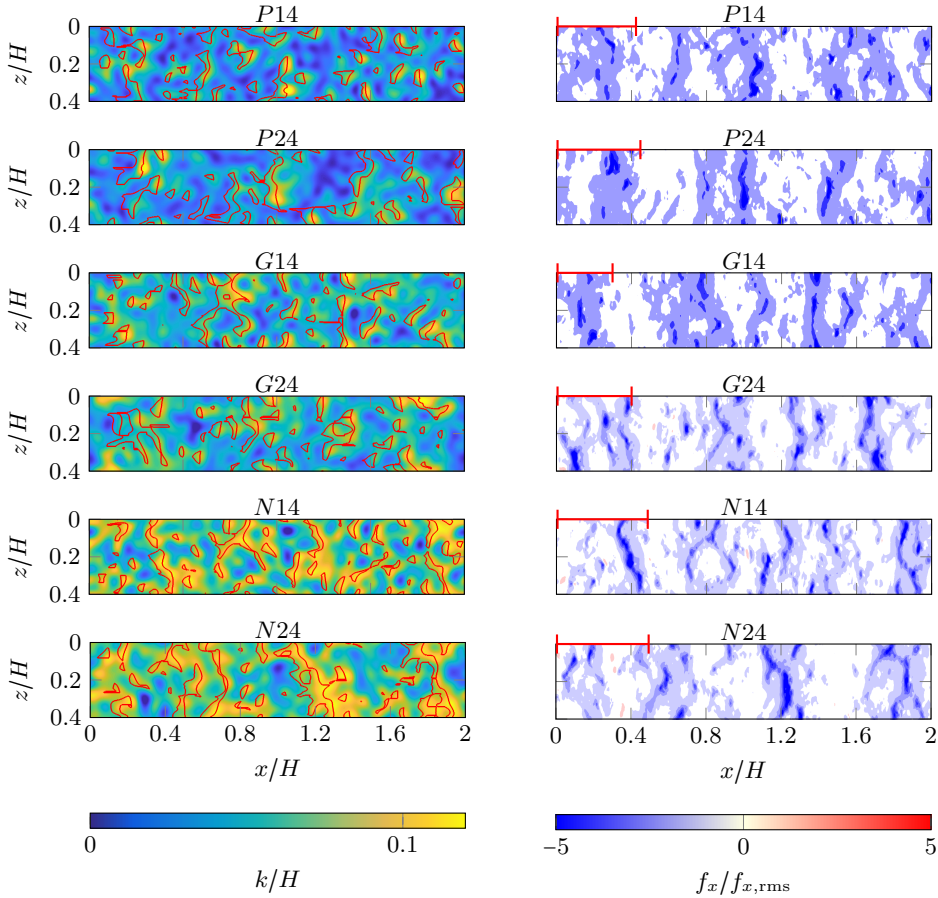


Figure 9: Roughness (left column) and surface force distribution (right column) pairs in $M2$. The exposed surface derived from the 1-D sheltering model is marked by red contour line on the roughness distribution maps. Separation lengths of force peaks obtained from the auto-correlation are represented by the red bars on the upper left corner of the surface force maps.

figure 9. The entire set of surface force distributions show spanwise-elongated coherent areas of negative forcing. Furthermore, force distributions in streamwise direction at $z = 0.2H$ are displayed for three cases $N24M2-500$ (negative skewness), $G24M2-500$ (Gaussian) and $P24M2-500$ (positive skewness) in figure 10 along with the surface height functions at the same location. In this figure, solid blue line represents the normalized negative force profile, $-f_x/f_{x,rms}$, while dashed red line represents the corresponding normalized roughness profile, k/k_{rms} . Comparing different roughness topographies, it can be observed that the Gaussian surface demonstrates a larger number of extreme force peaks than the surfaces with asymmetric PDF. As expected, the peaks in surface force are mostly collocated with the peaks in roughness height. A sudden rise in the negative force is expected when the mean flow impinges on the windward side of the roughness element followed by a rapid drop on the leeward side, which is also observed in the figure. Interestingly, the force peaks are much narrower than the surface height peaks, which can be attributed to the separation of flow behind the roughness peak. Another

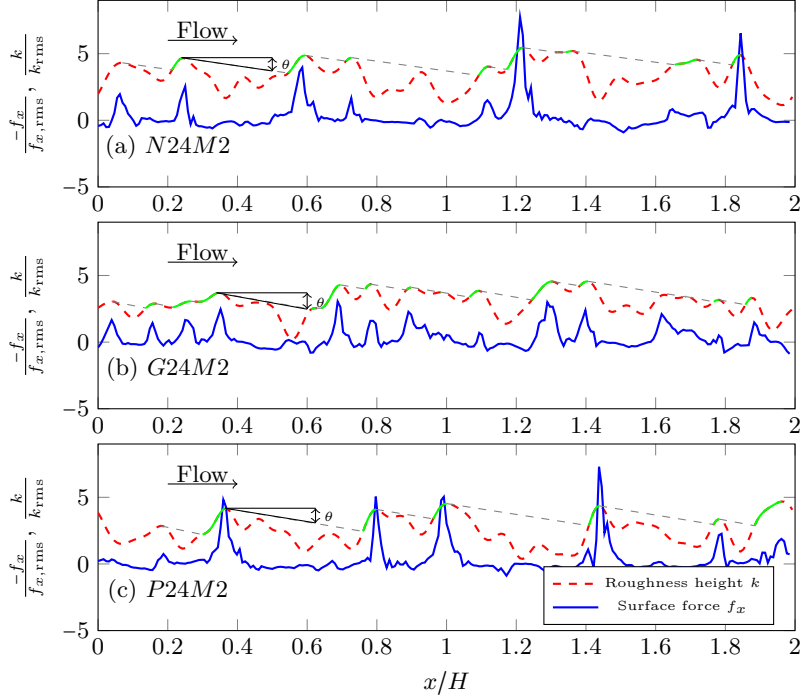


Figure 10: Normalized force f_x and roughness distribution profile for $N24M2$ (upper), $G24M2$ (middle) and $P24M2$ (lower) at $z = 0.2H$. Sheltering effect modeled by Yang *et al.* (2016) is illustrated by gray dashed lines, the unsheltered surfaces are marked by green profile.

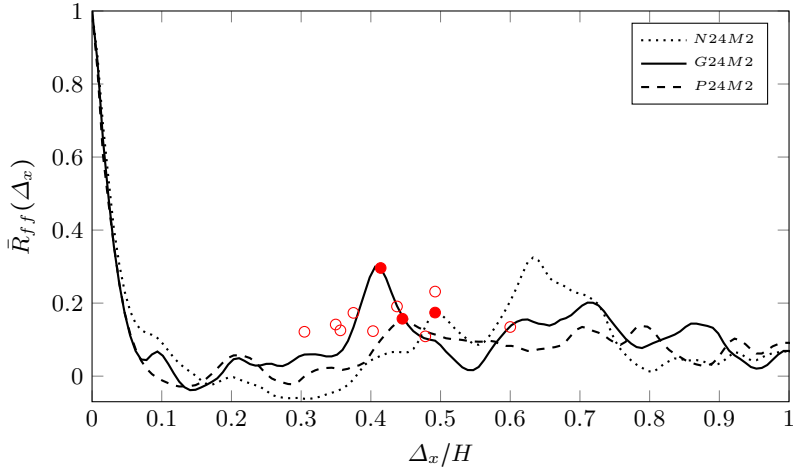


Figure 11: Auto-correlation function of the streamwise surface force component as a function of streamwise separation Δ_x . The first correlation peaks of the three auto-correlation functions are marked by red points, the peaks of the rest studied cases are marked by red circles.

notable observation is that the pronounced force peaks show a much longer streamwise separation than the height peaks. Such observation can be linked to the sheltering effect, which causes a significant reduction in the flow momentum in the wake of a tall roughness element.

Yang *et al.* (2016) investigated the sheltering effect on the surface roughened by rectangular-prism roughness elements and argued that once the region sheltered by the upstream roughness element covers the neighbouring elements, the surface drag decreases. They suggested that an attenuation parameter for skin friction should incorporate the ‘shadowed area’. To provide further insight into the present observations, we apply the wake expansion model proposed by these authors – with some simplification – to the roughness profiles in figure 10. According to Yang *et al.* (2016), the streamwise slope of the sheltered region from separation point down to the ground can be calculated from the wake expansion rate with $\tan \theta = C_\theta u_\tau / U_h$, where u_τ is the friction velocity, U_h is the velocity at roughness element height, $C_\theta = 1 - (2/3)(1 - h/w)$ is the shape parameter of the roughness and h/w denotes the aspect ratio of the rectangular prisms. With the aim to investigate the underlying physical mechanism of the sheltering model, we expand the use of the model – which is obtained based on rectangular prisms roughness – to more realistic irregular roughness. To approximate the expansion rate of irregular roughness in the present work we use double-averaged mean velocity at each roughness peak height as U_h . We also replace h with the characteristic roughness height $k_{99} = 0.1H$ and w with the spanwise integral length scale of the roughness $L_{k,z} \approx 0.05H$, which will be defined in the following section. Using these values, $C_\theta = 1.7$ is obtained and the resulting shadowed area in figure 10 is indicated by the gray dashed lines. In the same figure, the ‘exposed’ areas on the roughness peaks are highlighted by green lines. It is clear that the extreme force peaks coincide almost exclusively with the green areas and the shadowed areas rarely produce any significant local force. This can be an indication on the applicability of the wake expansion model to irregular roughness. The 1-D sheltering model is applied to the 2-D roughness distribution in figure 9. The exposed roughness surface are outlined by the red contour lines. One can observe that the exposed surface contours match well with the localization of the surface force. Notably, the spanwise elongated patterns of the surface force and their streamwise separation can be well reproduced with the help of sheltering model. This finding can also be an indication of the feasibility to predict the local drag with a knowledge of roughness structure, which has a predictive potential for more complex problems, e.g. inhomogenous and anisotropic roughness structures.

To shed further light on the surface force patterns and sheltering effect, the streamwise auto-correlation functions of the streamwise surface force $\bar{R}_{ff}(\Delta_x)$ for *N24M2*, *G24M2* and *P24M2* cases are shown in figure 11. The streamwise auto-correlation function of surface force is defined as

$$\bar{R}_{ff}(\Delta_x) = \frac{1}{L_x L_z} \int_0^{L_z} \int_0^{L_x} \frac{f_x(x, z)}{f_{x,\text{rms}}} \frac{f_x(x + \Delta_x, z)}{f_{x,\text{rms}}} dx dz . \quad (3.2)$$

A rapid drop of auto-correlation in the vicinity of zero separation – a result of the narrow peaks in the surface force distribution – is observed in figure 11. Additionally, a mild but clear positive peak in auto-correlation function, as marked by red circles, is observed at a separation of approximately $0.3-0.6H$. This value is likely to be related to the streamwise distance between the force peaks. Locations of the second auto-correlation peaks for the rest of studied cases are marked by hollow red circles in the same figure without showing the auto-correlation functions for better clarity. For visual comparison, we also indicate these values by red bars on the upper left corner of the respective surface force maps

Case	\bar{R}_{kf}	$\bar{R}_{kf,\text{exp}}$	Case	\bar{R}_{kf}	$\bar{R}_{kf,\text{exp}}$
P14M2 - 500	-0.46	-0.51	P18M1 - 500	-0.48	-0.54
P24M2 - 500	-0.48	-0.56	P28M1 - 500	-0.47	-0.56
G14M2 - 500	-0.44	-0.56	G18M1 - 500	-0.46	-0.56
G24M2 - 500	-0.44	-0.51	G28M1 - 500	-0.45	-0.59
N14M2 - 500	-0.38	-0.54	N18M1 - 500	-0.42	-0.55
N24M2 - 500	-0.41	-0.55	N28M1 - 500	-0.43	-0.57

 Table 5: Cross-correlation coefficient $\bar{R}_{kf}(\Delta = 0)$ and $\bar{R}_{kf,\text{exp}}(\Delta = 0)$

in figure 9. Here it can be confirmed that, roughly speaking, the length of the bars are similar to the separation between the spanwise-elongated areas with high surface force.

3.2.1. Correlation between surface force and roughness height

In this section, the link between streamwise component of surface force, $f_x(x, z)$, and roughness height distribution, $k(x, z)$ is analysed by means of correlation function of the two quantities. The correlation function $R_{kf}(\Delta_x)$ is calculated along the streamwise direction followed by averaging in the spanwise direction:

$$\bar{R}_{kf}(\Delta_x) = \frac{1}{L_x L_z} \int_0^{L_z} \int_0^{L_x} \frac{(k(x, z) - k_{\text{md}})}{k_{\text{rms}}} \frac{(f_x(x + \Delta_x, z) - \bar{f}_x)}{f_{x,\text{rms}}} dx dz, \quad (3.3)$$

where the subscript rms and overbar indicate root mean square value and mean value, respectively. The calculated values of correlation coefficient $\bar{R}_{kf}(\Delta_x = 0)$ for the studied topographies are summarized in Table 5. The negative sign of correlation indicates that high roughness peaks are correlated with negative surface force (force directed against the streamwise mean flow), as expected. It is observed that the negatively skewed topographies show lower correlation coefficient, which can be linked to the fact that this type of roughness is rather prone to generation of recirculation and separation zones in the surface valleys and indentations, so the responding force is less localized in those areas. Oppositely, for the positively skewed topographies higher correlation coefficients are observed due to the peak-dominated structures, in which the protruding parts of roughness are directly responsible for generation of localized drag force. The correlation coefficients of the exposed surface with the surface force distribution, $\bar{R}_{kf,\text{exp}}$, are also estimated and shown in table 5. Hereby only the exposed surfaces, i.e. the surface area that are marked by red contour lines in figure 9, are kept on the height map, while the sheltered surfaces are replaced by 0 elevation. Noticeable increase in the correlation coefficient can be observed for all cases, especially for negatively skewed roughness, where the correlation is increased by approximately 35%, while the increase for Gaussian and positively skewed roughness are 20% and 16%, respectively. This, once again, highlights the importance of sheltering effect and exposed roughness areas for the generation of surface force.

Furthermore, we calculate the integral length scales of streamwise surface force (L_f) and roughness height distribution (L_k). The integral length scales are calculated in a similar way as proposed by Quadrio & Luchini (2003) using the following expression for the integral length scale of roughness height

$$L_k = \int_{\Delta=0}^{L_{0,2}^{\text{corr}}} \bar{R}_{kk}(\Delta) d\Delta, \quad (3.4)$$

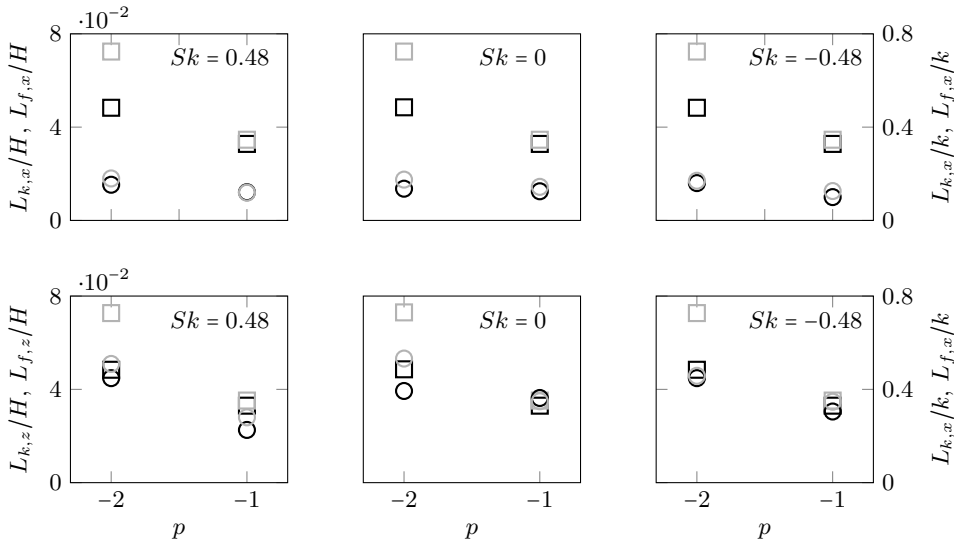


Figure 12: Integral length scale L_k and L_f as functions of p , grouped by Sk . Left axis: normalized by H , right axis: normalized by k . The squares represent L_k while circles represent the L_f . Black: $\lambda_0 = 0.8H$, gray: $\lambda_0 = 1.6H$. Upper row: streamwise integral length, lower row: spanwise integral length.

where Δ is the separation in either streamwise or spanwise directions and $L_{0,2}^{\text{corr}}$ is the separation at which the auto-correlation function drops under the arbitrary value of 0.2. The integral length scales for surface force L_f is computed in a similar fashion. The calculated values can be regarded as a scale for the width of roughness elements or force peaks. Both integral length scales are calculated for different cases and plotted in figure 12 as functions of topographical properties, i.e. PS slope p and λ_0 . In these figures, streamwise integral length scales are plotted on the upper row, while spanwise integral length scales are plotted on the lower row, grouped by Sk . Square symbols represent L_k while circles represent L_f . It is observed that surface force has a smaller streamwise integral length scale than the surface height, which is in line with the qualitative observation of the very narrow force peaks in figure 10. As expected, topographical parameters show a clear impact on the integral length scales of roughness height. Contrary to this, the streamwise integral length scale of force $L_{f,x}$ does not show strong sensitivity to the considered roughness variation. A notable observation is that the spanwise integral length scale of force $L_{f,z}$ is more sensitive to the topographical changes than the streamwise length scale. The value of $L_{f,z}$ is comparable to the surface height integral length scale $L_{k,z}$. Based on the limited data points in our dataset, the two quantities show similar trends with p and (to some extent) λ_0 : a higher value of $L_{f,z}$ is obtained for the roughness with $p = -2$ and $\lambda_0 = 1.6H$. Unlike the isotropic behavior of roughness height function, clearly illustrated by the comparable streamwise and spanwise integral length scales, the distribution of surface force is observed to be strongly anisotropic. The fact that the integral length scale of surface force is different in x - and z -directions is the quantitative manifestation of spanwise-elongated coherent areas of surface force observed in figure 9.

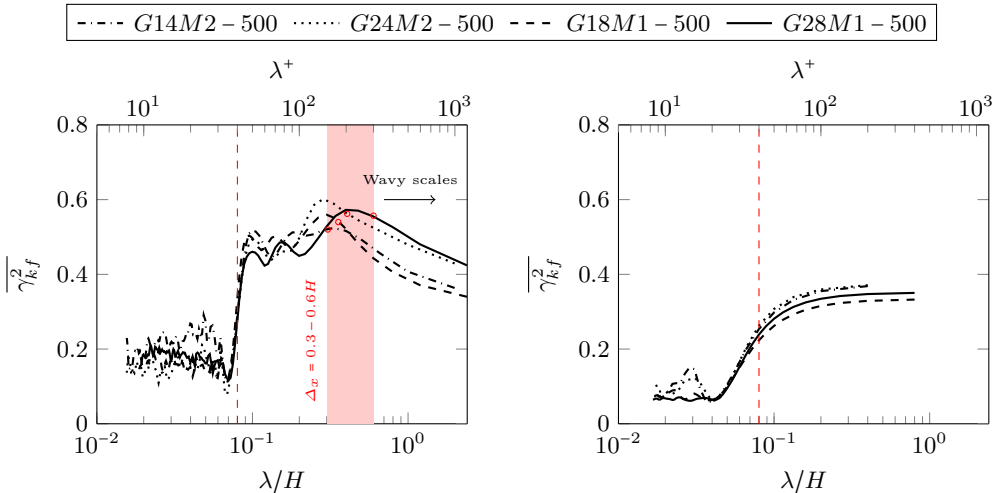


Figure 13: Mean coherence function $\bar{\gamma}_{kf}^2$ as a function of $\lambda = 2\pi/q$ normalized by H . Left: streamwise, right: spanwise. $\lambda_1 = 0.08H$ is marked by vertical dashed lines on the left and right side, respectively. λ^+ for the current cases $\text{Re}_\tau \approx 500$ is shown on the upper axis. The length scale of force separation obtained from its auto-correlation functions are marked by red circles on each coherence function respectively.

3.2.2. Coherence function of surface force and roughness

To further understand the correlation between force and height distributions at different roughness length scales, coherence function between the two distributions is calculated. The coherence function represents the correlation of force distribution with roughness height distribution as a function of wavenumber:

$$\bar{\gamma}_{kf}^2(q) = \frac{|E_{kf}(q)|^2}{E_f(q)E_k(q)}, \quad (3.5)$$

where $E_{kf}(q)$ represents cross-PS of roughness topography $k(x, z)$ and force map $f_x(x, z)$, while $E_f(q)$ represents the PS of $f_x(x, z)$. Power spectra are calculated based on 1D distribution profiles along streamwise and spanwise directions, and the mean coherence function $\bar{\gamma}_{kf}^2$ is obtained by averaging each parallel signal pairs. Figure 13 shows the mean coherence function of Gaussian surfaces in (a) streamwise direction and (b) spanwise direction as a function of wavelength $\lambda = 2\pi/q$ – upper axis shows inner scaled wavelength λ^+ at $\text{Re}_\tau = 500$. It is worth reminding that for all topographies, the smallest in-plane roughness scale is prescribed to be $\lambda_1 = 0.08H$. This is clearly related to the observation that coherence functions are significantly smaller below $\lambda \approx 0.08H$ ($\lambda^+ \approx 40$). Above this threshold, coherence functions increase and retain high values until a certain wavelength, which is roughly at $\lambda \approx 0.3 - 0.6H$ ($\lambda^+ \approx 150 - 300$) for the studied cases. With further evolution of the coherence function to larger wavelengths, the coherence decreases monotonically. Similar observations are made for negatively and positively skewed roughness. The force becomes less correlated with the surface features at very large scale, or in other words, very large wavelengths in streamwise direction do not contribute to the generation of surface force. These length scales might be related to the ‘wavy roughness’ concept stemming from the observations by Schultz & Flack

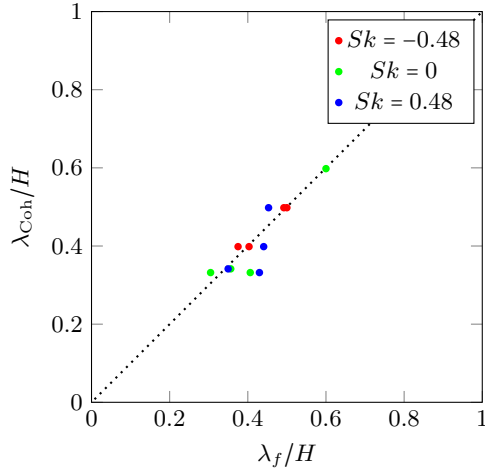


Figure 14: The length scale of force peak separation detected from the auto-correlation functions λ_f compared with the coherence dropping wavelength λ_{Coh} .

(2009). Barros *et al.* (2018) stated that these length scales can be filtered out in regard of determining the skin friction.

Notably, the streamwise wavelength at which the coherence starts to drop has a similar value to the streamwise separation distance of the surface force peaks. A comparison between the coherence dropping wavelength λ_{Coh} and the length scale of force peak separation λ_f is conducted in figure 14. It can be observed that all data points are clustering around $\lambda_{Coh} = \lambda_f$ (dotted line) indicating a clear correspondence of these length scales. The significant coherence at relative small length scales might be linked to the interaction of roughness structure and sheltering. As discussed before, the occurrence of extreme force peaks is strongly determined by the roughness areas that are exposed in the high-momentum flow, or outside the sheltering. Thus, streamwise recurring force peaks caused by sheltering can be found in figure 9. Less prominent force peaks can be found between two successive extreme peaks, which contributes to the coherence function at small wavelength. Furthermore, the roughness structures whose length scales are comparable to the distance between two successive extreme peaks, i.e. λ_f , show significance in the coherence function at corresponding wavelength. Beyond this length scale, no larger force peak separation can be found, the coherence function keeps decreasing into large wavelength region.

Figure 13(b) demonstrates that, unlike the tortuous behavior exhibited by the streamwise mean coherence function, the spanwise mean coherence function shows a monotonically increasing trend before a plateau at larger wavelengths.

3.3. Effect of topographical properties

In section 3.1.3, we discussed the applicability of minimal channel concept for characterization of realistic roughness. In doing so, we examined a relatively large number of roughness topographies. This provides a basis for studying the effect of roughness topography on hydrodynamic properties of the surface, here ΔU^+ and d^+ . The present section is devoted to this task. As discussed in previous sections, minimal channels are capable for indicating the hydrodynamic behaviour of roughness. Thus, the bold values in table 3, which are regarded as the minimal channel results, will be used in this section.

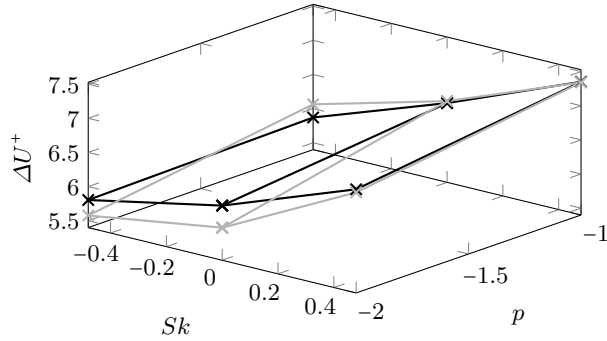


Figure 15: ΔU^+ prediction from minimal channels, black: $\lambda_0 = 0.8H$, gray: $\lambda_0 = 1.6H$

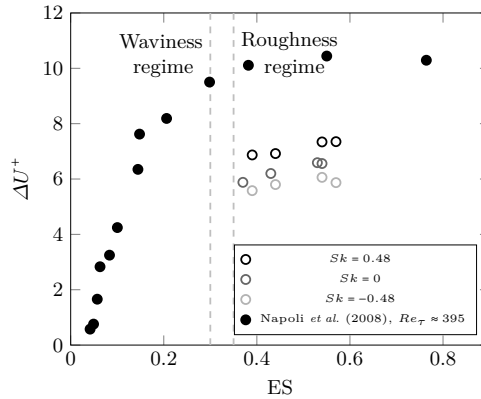


Figure 16: ΔU^+ as a function of ES. The distinction between waviness and roughness regimes as suggested by Schultz & Flack (2009) is indicated by vertical dashed lines.

3.3.1. Roughness function

An overview of the roughness function ΔU^+ from minimal channel simulations is plotted in figure 15, where roughness function ΔU^+ is shown as a function of two of the investigated roughness parameters, i.e. skewness Sk and PS slope p . The PDFs of the considered topographies are shown in figure 2(a). In figure 15 the corresponding effect of Sk on the retardation of mean velocity profile is shown. As investigated by Flack *et al.* (2020), positively skewed rough surfaces give higher skin friction than non-skewed or negatively skewed roughness. Negatively skewed surfaces show 'slip-velocity' effect (Jelly & Busse 2018), which translates into a lower mean velocity retardation. The trend observed in the present results fully agrees with what suggested by the previous researchers.

In general, ΔU^+ reaches a higher value with $p = -1$. As illustrated in figure 2(b), at $p = -2$ larger wavelengths contribute more to the roughness and at $p = -1$ *vice versa*. These findings agree with the study by Barros *et al.* (2018) and section 3.2 highlighting, that relative small length scales of roughness have a dominant role in determining hydraulic drag. Furthermore, it can be observed that the surfaces with $\lambda_0 = 1.6H$ show stronger sensitivity to the change of PS slope p than those with $\lambda_0 = 0.8H$. Moreover, it can be observed in figure 15 that ΔU^+ generally decreases with increasing λ_0 . So far we have discussed the effect of three parameters directly prescribed in the present work, i.e. Sk , p and λ_0 . ES is another roughness metric, which is widely discussed in the literature

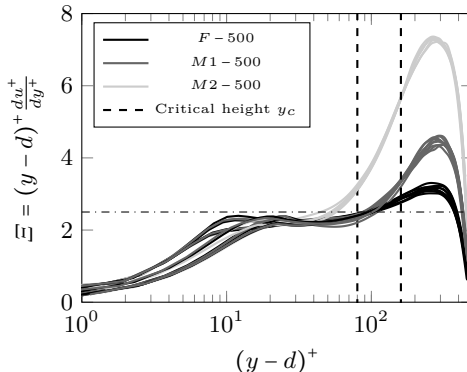


Figure 17: Log-law diagnostic function, horizontal dash-dotted line represents $\bar{\Xi} = 2.5$, vertical dashed lines shows the critical height $y_c^+ = 80, 160$ for $M2-500$ and $M1-500$, respectively.

and used in roughness correlations. Even though ES is not explicitly prescribed in the present work, it is indirectly varied due to variation of other parameters. ES is particularly controlled by the two PS parameters p and λ_0 , which means that by varying these two parameters we implicitly study the effect of ES on the roughness function. In figure 16 the correlation of ΔU^+ and ES can be directly observed for the present data. It is observed, that for all values of Sk , ΔU^+ increases with ES. The slight drop of the last data point for Gaussian and negatively skewed roughness is likely due to the skimming effect of 'pit-dominant' surface with rapid surface sinking illustrated by the high ES.

Since all the present roughness topographies have an $ES > 0.35$ they can be considered as roughness and not waviness surfaces according to the classification by Flack & Schultz (2010). It is previously shown, e.g. by Napoli *et al.* (2008), that roughness function only increases moderately with ES in this range, which agrees well with the presently observed trend. As a reference, the data obtained at $Re_\tau \approx 395$ by Napoli *et al.* (2008) are plotted in the same figure, in which irregular roughness are represented by superposition of different sinusoidal waves with random amplitude. It is observed in the figure that, although the trend of ΔU^+ with ES is similar in the present and the reference data, there are large offset between different groups of data points. It indicates that (obviously) roughness function is not uniquely determined by ES.

Although the trend in the results can be qualitatively explained by selected roughness statistics based on the previous research, it is also shown that predicting skin friction based on roughness statistics is incomplete. By observing the roughness statistics in table 1 and the corresponding simulation results in table 3, the prediction of the skin friction coefficient solely based on limited amount of statistical properties seems to be rather different. Different types of roughness with similar statistical properties, e.g. the roughness with same values of Sk and k_{rms} in table 1, show significant variation of their ΔU^+ values. A better correlation for ΔU^+ is observed when ES is added to the picture. However, inclusion of ES is still not necessarily expected to yield unique predictions. A simple illustrative example could be that roughness formed by staggered and aligned roughness elements with identical statistics can lead to a significantly different values of in k_s , as shown in the study by Forooghi *et al.* (2017).

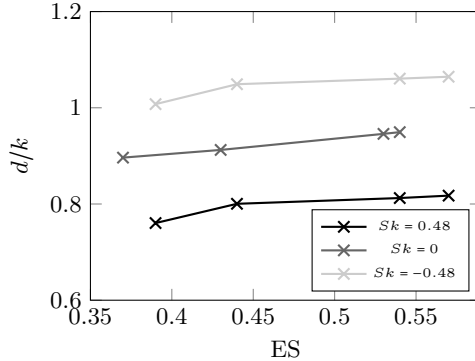


Figure 18: d predictions as a function of ES, grouped by Sk .

3.3.2. Zero-plane displacement

As discussed before due to the rough structures, the logarithmic layer of the flow is shifted upwards to the fluid. Thus, the origin of wall-normal coordinate cannot be defined *a priori*. As a result it is necessary to use a physically justified virtual origin for the logarithmic law of the wall. The virtual origin lies above the $y = 0$ plane at a distance equal to zero-plane displacement d . In order to investigate if the present choice of virtual wall leads to a satisfactory logarithmic behavior, diagnostic functions $\Xi = (y-d)^+ du^+/dy^+$ are shown in figure 17. The constant value of $\Xi \approx 2.5$ is expected in the logarithmic region. One should note that, due to the limited extend of ‘healthy turbulence’ in minimal channels, logarithmic profile is only expected to exist under the critical height y_c . Hence, it is observed that with decreasing the channel size, the diagnostic functions deviate from those of the full channel simulations beyond y_c . The value of zero-plane displacement d/k are documented in table 3. To summarize the effect of roughness topography on zero-plane displacement d/k is plotted as a function of effective slope ES in figure 18, while the data points are grouped by Sk . It can be observed that the value of d/k increases with an increase in ES and a decrease in Sk , while the skewness effect is more dominant. For the cases with negative Sk $1 < d/k < k_t/k$ so that the zero plane displacement is still below the maximum roughness height.

3.4. Assessment of existing roughness correlations

In this section, results from previously introduced topographies at $k^+ \approx 50$ are used to assess some of the existing roughness correlations. As a matter of fact, existing roughness correlations are developed based on a limited number of data points covering a certain region of the parameter space (Chung *et al.* 2021). In this section, we are particularly interested to shed light on the generalization of these correlations outside their original parameter space, which is a key for a correlation to work across a wide range of rough surfaces encountered in different applications. Furthermore, this section aims at developing a general idea of the reliance of roughness characterization on particular statistical measures of roughness. Therefore, we adapted the constants from their original publications without fitting them to the present testing dataset. There are in general two types of roughness correlations in literature, those directly predicting the equivalent sand-grain roughness k_s and those predicting the roughness function ΔU^+ . The latter group is more suitable for the transitionally rough regime since k_s is essentially defined when the flow is fully rough. In the following we first assess three correlations (Eqn. 3.6, Eqn. 3.7 and Eqn. 3.8) developed based on transitionally and fully rough data and then

examine two correlations (Eqns 3.9 and 3.10) specifically developed for the fully-rough regime. It was shown in the previous sections that a fully rough regime for the surfaces under investigation is likely reached at about $\Delta U^+ > 6$. However, in the present section we calculate the equivalent roughness height based on ΔU^+ for all cases, including those with values of roughness function smaller but close to 6. It must however be kept in mind that k_s is only a relevant quantity in the fully rough regime. Figure 19 visualizes the selected correlations, where parameter space covered by fitting data of each correlation is represented by a red frame. In each sub-figure the data points from the present work are depicted as symbols. Different symbol colors are used to make distinction between the data points lying inside and outside the fitting region. Here the parameter space is expressed in terms of the two widely used parameters Sk and ES, even though they both may not explicitly appear as predictive parameters in all correlations.

Required roughness statistics of the present roughness topographies are listed in Table 1. First we examine the correlation proposed by Chan *et al.* (2015), which is based on 3D sinusoidal roughness data in both transitionally and fully rough regimes. These authors proposed expressions for ΔU^+ and k_s as follows.

$$\Delta U^+ = \frac{1}{\kappa} \log(k_a^+) + 1.12 \log(\text{ES}) + 1.47, \quad (3.6)$$

$$k_s = 7.3 k_a \text{ES}^{0.45}. \quad (3.7)$$

We visualized only one of these two related correlations in figure 19 (a). The data points from the present work locate in the range of fitting data except for the topographies with $Sk < 0$. Obviously, since Sk is not used as a predictive parameter in these correlations, they returns same predictions for different values of Sk .

Thakkar *et al.* (2017), developed a correlation based on a roughness parameter λ_T including a wider range of primary topographical parameters. Their correlation is developed in transitionally rough regime, thus only ΔU^+ is predicted. In this correlation, ΔU^+ is linearly related to λ_T :

$$\Delta U^+ = \alpha_T \lambda_T + \beta_T, \quad (3.8a)$$

$$\lambda_T = \ln\left(\frac{S_f}{S}\right) \left[1 + 0.09 \ln\left(\frac{L_x^{\text{corr}}}{k_{t,5 \times 5}}\right)\right] \left(\frac{4k_{\text{rms}}}{k_{t,5 \times 5}}\right)^{-0.44} e^{(-0.074Sk)}, \quad (3.8b)$$

where $\alpha_T = 1.4699$ and $\beta_T = 8.0394$ represent empirical parameters. S_f/S is the ratio of the total frontal projected area and wall-normal projected area of the roughness. L_x^{corr} is the correlation length of roughness, at which length scale auto-correlation of roughness drops to 0.2. $k_{t,5 \times 5}$ is the peak-to-trough height averaged over 5×5 uniform subsets of the surface. The prediction of ΔU^+ by this correlation is shown in figure 19(b) as a function of Sk and ES.

It can be observed from figure 19(b), that all the data from the present work locate outside of the fitting data in terms of Sk and ES. Furthermore, two correlations specifically aimed at fully-rough regime are examined. These are the correlation by Forooghi *et al.* (2017)

$$k_s = k[0.67Sk^2 + 0.93Sk + 1.3][1.07(1 - e^{-3.5\text{ES}})], \quad (3.9)$$

and the one by Flack *et al.* (2020),

$$\begin{cases} k_s = 2.73k_{\text{rms}}(2 + Sk)^{-0.45}, & Sk < 0, \\ k_s = 2.11k_{\text{rms}}, & Sk = 0, \\ k_s = 2.48k_{\text{rms}}(1 + Sk)^{2.24}, & Sk > 0. \end{cases} \quad (3.10)$$

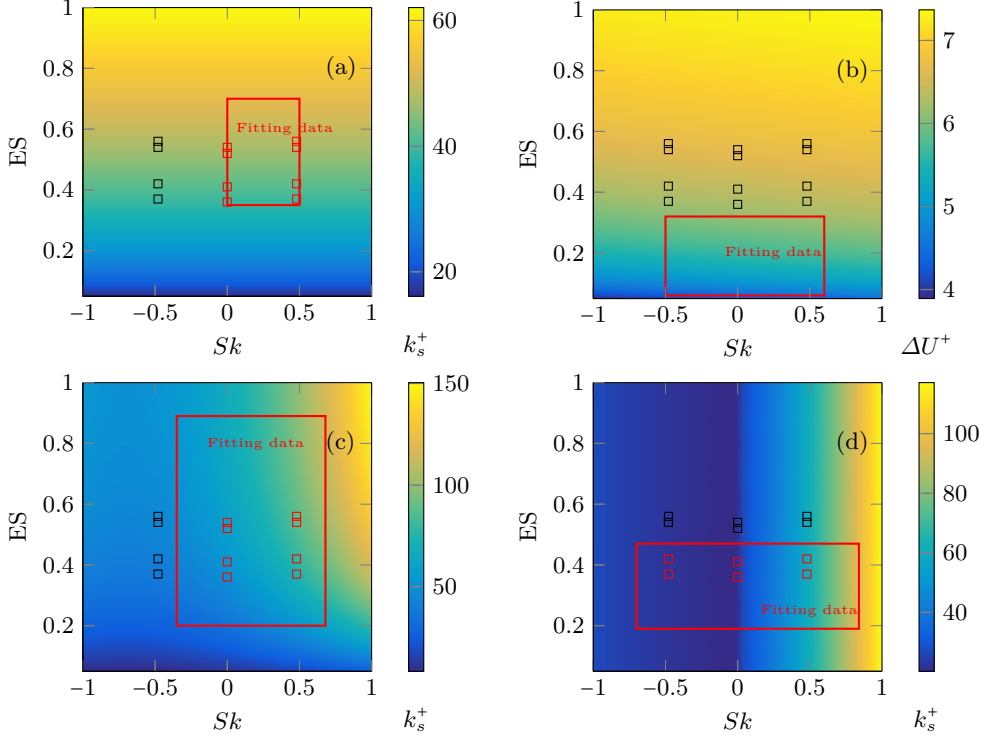


Figure 19: Predictive correlations of k_s^+ and ΔU^+ . Squares indicate data points from present work while red frame represents the fitting data from literature. $S_f/S = 0.25$, $L_x^{\text{corr}} = 0.08H$, $k_t = 0.12H$, $k_{\text{rms}} = 0.02H$, are chosen to be comparable with the present roughness dataset. (a): Eqn. 3.7 by Chan *et al.* (2015), (b): Eqn. 3.8 by Thakkar *et al.* (2017), (c): Eqn. 3.9 by Foroughi *et al.* (2017), (d): Eqn. 3.10 by Flack *et al.* (2020).

Predictions of ΔU^+ and k_s^+ from all proposed correlations are summarized in table 6 and table 7, respectively. In order to directly evaluate the models, ΔU^+ and k_s^+ predicted by correlations are normalized and plotted against the full-span DNS results in figure 20(a,b). The equivalent sand grain sizes k_s^+ of roughness from the simulations are obtained by fitting roughness function to the fully-rough asymptote, i.e. Eqn. 2.9. One should recall that the present data points cover both transitionally and fully rough regimes, while the correlations in question (except one) are specifically developed for one of the regimes. While acknowledging this we apply each correlation for prediction of all data points to assess the exportability of the correlations. Obviously, in figure 20 the fully rough regime is approached as ΔU^+ increases. Based on the result in section 3.1.4, an approximate value of $\Delta U^+ \approx 6$ corresponding to $k_s^+ \approx 50$ is regarded as the threshold of fully-rough regime and indicated by vertical dashed lines in figure 20. It has to be mentioned that this value is an approximate criterion to estimate the roughness regime. Exact ΔU^+ criterion for different types of roughness can only be achieved through comprehensive experiments. Interestingly, while the transitional correlations show a declining accuracy in figure 20(a), no sharp degradation in their prediction is observed when entering the fully rough regime.

Topography	ΔU_{DNS}^+	$\Delta U_{\text{Eqn.3.6}}^+$	$\Delta U_{\text{Eqn.3.8}}^+$
P14	7.33	6.06 (-17.3%)	6.09 (-16.9%)
P18	7.23	6.00 (-17.0%)	6.04 (-16.5%)
P24	6.99	5.77 (-17.5%)	5.51 (-21.2%)
P28	6.57	5.64 (-14.2%)	5.19 (-21.0%)
G14	6.67	5.85 (-12.3%)	5.89 (-11.7%)
G18	6.56	5.83 (-11.1%)	5.82 (-11.3%)
G24	6.30	5.60 (-11.%)	5.27 (-16.3%)
G28	5.94	5.43 (-8.6%)	4.92 (-17.2%)
N14	6.14	6.06 (-1.3%)	5.94 (-3.3%)
N18	6.09	6.00 (-1.5%)	5.89 (-3.3%)
N24	5.82	5.77 (-0.9%)	5.32 (-2.1%)
N28	5.51	5.64 (+2.0%)	4.98 (-9.6%)

Table 6: Prediction of ΔU^+ by Chan *et al.* and Thakkar *et al.*. Values in the brackets are the relative errors to the DNS results.

Topography	$k_{s,\text{DNS}}^+$	$k_{s,\text{Eqn.3.7}}^+$	$k_{s,\text{Eqn.3.10}}^+$	$k_{s,\text{Eqn.3.9}}^+$
P14	69.69	48.18 (-30.9%)	62.07 (-10.9%)	87.86 (+26.1%)
P18	66.95	47.02 (-29.8%)	62.07 (-7.3%)	86.33 (+28.9%)
P24	60.82	42.88 (-29.5%)	62.07 (+2.1%)	79.89 (+31.4%)
P28	51.42	40.62 (-21.0%)	62.07 (+20.7%)	75.72 (+47.3%)
G14	53.52	44.26 (-17.3%)	21.10 (-60.6%)	59.04 (+10.3%)
G18	51.21	43.89 (-14.3%)	21.10 (-58.8%)	58.67 (+14.6%)
G24	46.15	39.95 (-13.4%)	21.10 (-54.3%)	54.11 (+17.2%)
G28	39.96	37.33 (-6.6%)	21.10 (-47.2%)	50.50 (+26.4%)
N14	43.29	48.18 (+11.3%)	23.52 (-45.7%)	32.32 (-25.3%)
N18	42.44	47.02 (+10.8%)	23.52 (-44.6%)	31.76 (-25.2%)
N24	38.09	42.88 (+12.6%)	23.52 (-38.3%)	29.39 (-22.8%)
N28	33.65	40.62 (+20.7%)	23.52 (-30.1%)	27.86 (-17.2%)

Table 7: Prediction of k_s by Chan *et al.*, Flack *et al.* and Forooghi *et al.*. Values in the brackets are the relative errors to the DNS results.

In figure 20(b) different error intervals in prediction of k_s^+ are illustrated by green shades. One should recall that, according to Eqn. 2.9, there is a logarithmic relation between ΔU^+ and k_s^+ . Therefore, for the sake of comparability, error intervals for ΔU^+ corresponding to 10%, 20% and 30% k_s error at $k_s^+ = 60$ are calculated from Eqn. 2.9 and illustrated in figure 20(a) using the same green shades. In general, a similar range of error can be observed among prediction of all correlations in both figure 20 (a & b) where a limited number of data points lie outside the 30% k_s error area. The fact that none of the correlations are able to perfectly reproduce the effect of topography on k_s - as already pointed out by other authors (Flack *et al.* 2020) - can be acknowledged in figure 20. Among all correlations, the ones by Chan *et al.* and Flack *et al.* incorporate less geometrical information by taking one parameter related to the topography each, namely the effective slope of roughness in the former and the skewness in the latter. Forooghi *et al.* combined both approaches and Thakkar *et al.* examined an even wider range of topographical properties related to both PDF and PS. While the latter two models

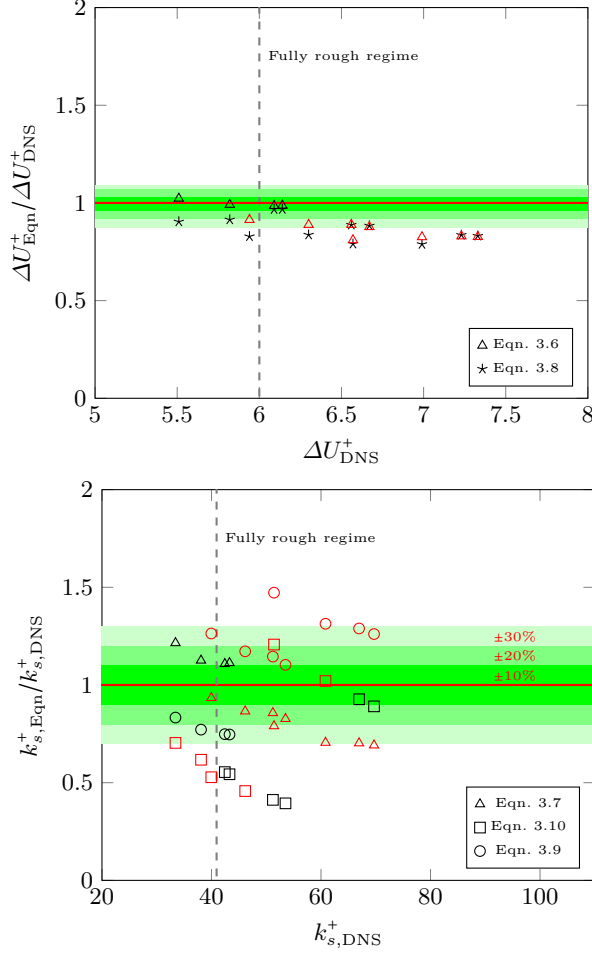


Figure 20: Prediction of ΔU^+ (upper figure) and k_s^+ (lower figure) vs. simulation. red symbols indicate the present data points that locate within the fitting dataset. In (b) 10%, 20% and 30% error intervals are represented by green shadow. In (a) the error intervals of ΔU^+ correspond to 10%, 20% and 30% error of k_s^+ at $k_s^+ = 60$.

deliver better predictions for some data points, an obviously superior accuracy cannot be established. One notable observation from all correlations is that their prediction does not deteriorate particularly for the data outside their original fitting range. This can be an indication that either of the models can be used with a similar level of reliability in a wider parameter space that is originally designed for. Obviously, this statement is unlikely to hold for extreme cases outside the scope of this paper.

To summarize, this section highlights the need for a more general model, e.g. by taking advantage of advances in data-driven methods. For the future development of roughness models/correlations, it is suggested by the present work that the roughness statistics that contain both height distribution and horizontal scales of roughness need to be incorporated for generalizable predictions.

4. Conclusion

DNS is carried out for turbulent flow over irregular roughness in plane channels with reduced stream- and spanwise extents – referred to as minimal channels. Roughness topography is mathematically generated using the method proposed by Pérez-Ràfols & Almqvist (2019), in which PDF and PS of roughness map can be prescribed with high precision. Simulation has been run for 12 different roughness topographies at $k^+ = 50$ and for a selected topography at $k^+ = 25 - 100$. For all cases, solutions are produced in full channels and one or more minimal channels. It is systematically demonstrated that, the value of roughness function for an irregular roughness with random nature can be predicted within $\pm 5\%$ error using DNS in a minimal channel. The stream- and spanwise size of minimal channel must be larger than 1000 and 100 in wall units, respectively, and roughness sublayer must be within $0.4L_z$ wall distance similar to what suggested by previous authors (Chung *et al.* 2015; MacDonald *et al.* 2017) for regular sinusoidal roughness. Present results also suggest that minimal channels yield accurate prediction as long as – in addition to the previous conditions – the size of channel is large enough to accommodate more than 90% of original roughness height spectral energy based on the area under 2D PS. This finding is particularly relevant in DNS-based characterization of realistic rough surfaces that may contain very large wavelengths with limited contributing to the root mean square roughness height. To shed more light on possible origins of the mild discrepancy between minimal and full channel results, for one topography, multiple rough surfaces are generated. Due to random nature of roughness generation process, these surfaces are deterministically different while statistically identical. Simulations are carried out for these surfaces with $k^+ = 50$ and slightly scattered values of roughness function are obtained. Notably, roughness function value for the full channel resides within 99% uncertainty interval of these scattered predictions. The results indicate that, at fixed PDF and PS, randomness in roughness generation can lead to a small uncertainty, which is also likely the origin of the observed $\pm 5\%$ discrepancy between predictions of minimal and full channels. Thus, a new perspective of more accurately characterizing the roughness using the roughness PDF and PS is proposed in the present work.

In addition to global flow properties, local surface forces for different types of roughness are calculated and their correlations with respective roughness height functions are studied. It is found that peaks of surface force clearly correlate with roughness peaks. Such a correlation is not observed at roughness troughs, which is at least partly responsible for a reduced cross-correlation coefficient between the two functions for negatively skewed roughness topographies. It is also observed that not all roughness height peaks generate force peaks. Applying the sheltering model proposed by Yang *et al.* (2016) with some assumptions, we are able to show that only ‘exposed’ (unsheltered) roughness peaks generate prominent peaks in surface force. Notably, the spanwise elongated patterns of the surface force and their streamwise separation can be well reproduced with the help of the sheltering model. This can be taken as a clear indication of the relevance of sheltering effect in flow over stochastic roughness – e.g. for complex terrains.

Furthermore, it was revealed that integral length scale of the force distribution in streamwise direction is meaningfully smaller than that of roughness height function and shows little sensitivity to the topographical features of the surface. This can be attributed to the formation of wake behind roughness peaks leading to sharp drop of surface force on the leeward side of the peak. We also studied the coherence function of roughness height and force power spectra as a function of streamwise and spectral scales. In streamwise direction, it was observed that coherence starts dropping beyond a certain length. This observation can be interpreted as smaller contribution of very large

roughness wavelengths to the drag force. These large roughness length scales might be related to the ‘wavy roughness’ concept stemming from the previous studies. Notably, the wavelength at which the coherence starts dropping is shown to be related to the separation between the peaks of surface force, which is linked to the sheltering effect itself. Unlike the streamwise direction, the coherence function does not drop in spanwise direction for the cases studied in this paper.

As stated above, present results suggest that an accurate yet computationally economical framework for characterization of irregular, realistic rough surfaces is in hand. Such a framework, can for example, be a basis for generation of large databases required for future ‘data-driven’ roughness correlations. While this can be considered an obvious future research direction, in the present paper, we used the results from the 12 simulated roughness topographies to study the dependence of roughness function as well as zero-plane displacement on some key roughness parameters. Notably, it was shown that normalized zero plane displacement d/k is most sensitive to the skewness of roughness distribution (larger at smaller values of skewness), and it also mildly increases with effective slope.

Finally we assessed a number of widely cited roughness correlations in the literature (Eqns. 3.6-3.10). While some correlations show a certain level of success in reproducing the roughness function or equivalent sand-grain roughness compared to the DNS results (see figure 20), there is an obvious need for improvement. An interesting observation is that none of the assessed correlations show a dramatic loss of accuracy when used outside the parameter space of its original fitting data. However, even the most successful correlations, can only reproduce the DNS data within $\pm 30\%$ accuracy. This can arguably be the ground for a paradigm shift in development of future roughness correlations. As mentioned before a data-driven approach, which can account for the stochastic nature of roughness and its interaction with near-wall turbulence may be a solution to this problem. Recently, this idea has received some attention (Aghaei Jouybari *et al.* 2021) and more work in this direction is called for.

Acknowledgements

Jiasheng Yang and Pourya Forooghi gratefully acknowledge financial support from Friedrich und Elisabeth Boysen-Foundation (BOY-151). This work was performed on the supercomputer ForHLR and the storage facility LSDF funded by the Ministry of Science, Research and the Arts Baden-Württemberg and by the Federal Ministry of Education and Research.

Declaration of interests

The authors report no conflict of interest.

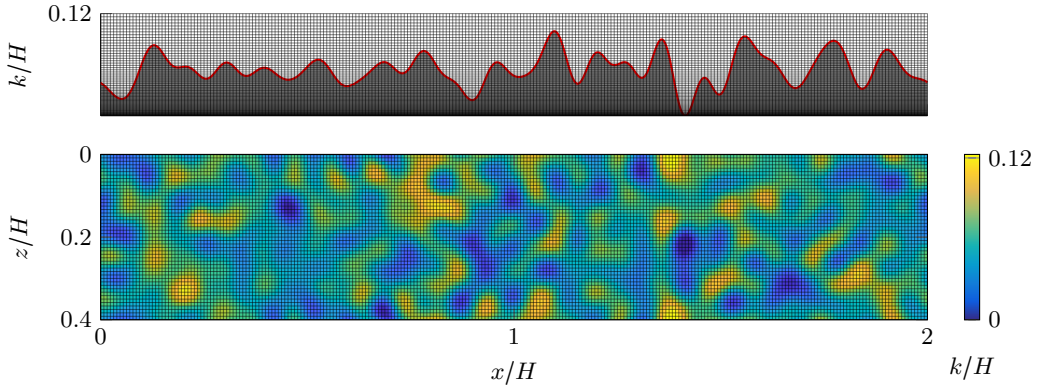


Figure 21: Mesh visualization in the wall layer with rough surface $G14M2-500$. Upper: mesh in wall-normal direction along $z = 0.2H$. Lower: mesh in wall-parallel direction.

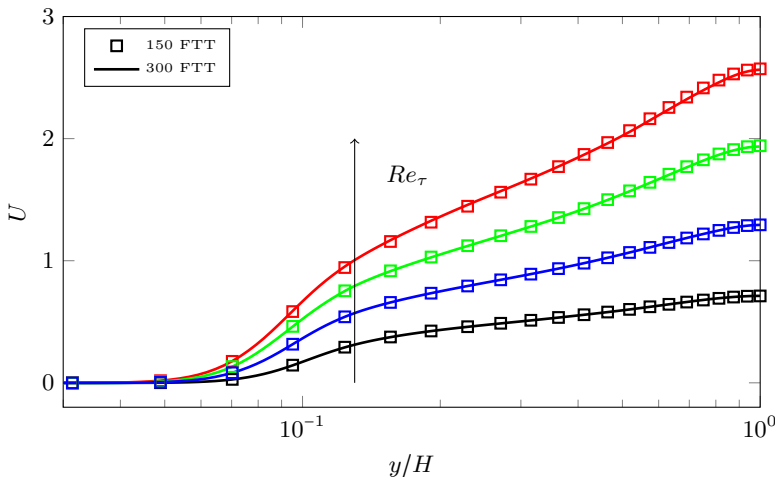


Figure 22: Statistical convergence of minimal channel M1s, color indicates different $Re_\tau = 250, 500, 750, 1000$. Lines: 300 FTT, squares: 150 FTT

Appendix A. Visualization of grid resolution

In the present work, IBM is employed to introduce the roughness into the simulation flow field. With the help of IBM the complex geometry of the roughness can be represented on simple Cartesian grid. However, in order to completely represent the roughness with Cartesian grid, sufficiently fine grid resolution is essential. The grid resolution in the present work is illustrated in figure 21, where one of the rough surfaces with the smallest correlation length L_x^{corr} , i.e. $G14M2-500$ is shown. This rough surface contains the finest roughness structure among all the cases.

Appendix B. Convergence test of integration time

In order to determine the appropriate integration time for converged mean velocity profile, mean velocity profiles over roughness $G24M1$ at 4 different Re_τ averaged with 150 and 300 FTTs are compared and shown in figure 22. The profiles obtained with 150

FTTs at 4 different Re_τ collapse to the 300 FTTs profiles. On the other hand, MacDonald *et al.* (2017) estimated the convergence of mean velocity profile in minimal channels in terms of the count of captured y_c -sized eddies during the simulation. The number of captured eddies can be expressed as

$$C^* = \frac{T_{sim} u_\tau}{6y_c} \frac{L_y}{H} \frac{L_x}{7.5y_c} \frac{L_z}{2.5y_c},$$

Where T_{sim} is the total simulation time, $y_c = 0.4L_z$ is the critical height of the minimal channels. The 95% confidence interval of the ΔU^+ prediction is formulated as $\Delta U^+ \pm \epsilon^+$ where: $\epsilon^+ \approx 91.4(C^*)^{-1/2}/y_c^+$. The current criteria of 300 FTTs corresponds to $\epsilon^+ \approx 0.07$, 0.07, 0.05 and 0.03 for minimal channel $M1$ at $Re_\tau = 250, 500, 750$ and 1000, respectively. Thus the integration time of minimum 300 FTTs in the present work is shown long enough for achieving converged mean velocity profile.

Appendix C. Definition of zero-plane displacement

The zero-plane displacement d , according to Jackson (1981), is placed at the centroid of the distributed drag on the roughness surface. The moment of the drag can be calculated by projecting the drag forces on a y - z plane. However, it is demonstrated by this author that d can be calculated in terms of mean flow properties, i.e. total shear stress τ_{tot} . The time averaged Navier-Stokes equation of the flow in streamwise direction writes:

$$\rho \frac{\partial(\bar{u}\bar{u})}{\partial x} + \rho \frac{\partial(\bar{u}\bar{v})}{\partial y} + \rho \frac{\partial(\bar{u}\bar{w})}{\partial z} = -\frac{\partial\bar{p}}{\partial x} + \frac{\partial T_{11}}{\partial x} + \frac{\partial T_{12}}{\partial y} + \frac{\partial T_{13}}{\partial z} - P_x + \bar{f}_{x,IBM}, \quad (4.1)$$

where \bar{u} , \bar{v} and \bar{w} are the mean velocity components. \bar{p} is the mean pressure and T_{11} , T_{12} and T_{13} are the stresses including Reynolds stresses. $\bar{f}_{x,IBM}$ is the streamwise component of the mean IBM force. P_x is the constant pressure gradient added to the flow. With the idealized geometry proposed by Jackson (1981), if (4.1) is integrated over wall-parallel directions, then multiplied by y and integrated over y from the bottom $y = 0$ to the tip of the roughness $y = k_t$ we obtain:

$$\begin{aligned} & \underbrace{\int_{L_z} \int_0^{k_t} y \rho [\bar{u}\bar{u}]_0^{L_x} dy dz}_{=0} + \int_{L_z} \int_{L_x} [y \rho \bar{u}\bar{v}]_0^{k_t} dx dz - \int_{L_z} \int_{L_x} \int_0^{k_t} \rho \bar{u}\bar{w} dy dx dz \\ & + \underbrace{\int_{L_x} \int_0^{k_t} y \rho [\bar{u}\bar{w}]_0^{L_z} dy dx}_{=0} = \underbrace{\int_{L_z} \int_0^{k_t} -y [\bar{p}]_0^{L_x} dy dz}_{=0} + \underbrace{\int_{L_z} \int_0^{k_t} y [T_{11}]_0^{L_x} dy dz}_{=0} \\ & + \int_{L_z} \int_{L_x} [y T_{12}]_0^{k_t} dx dz - \int_{L_z} \int_{L_x} \int_0^{k_t} T_{12} dy dx dz + \underbrace{\int_{L_x} \int_0^{k_t} y [T_{13}]_0^{L_z} dy dx}_{=0} \\ & - \int_{L_z} \int_{L_x} \int_0^{k_t} y P_x dy dx dz + \int_{L_z} \int_{L_x} \int_0^{k_t} y \bar{f}_{x,IBM} dy dx dz. \end{aligned} \quad (4.2)$$

As marked in the equation, some of the terms vanish due to the periodic boundary condition in wall parallel directions. Thus, the moment of the drag acting on the

roughness writes:

$$M = - \int_{L_z} \int_{L_x} \int_0^{k_t} y \bar{f}_{x, \text{IBM}} dy dx dz = \int_{L_x} \int_{L_z} [y T_{12} - y \rho \bar{u} \bar{v}]_{y=k_t} dz dx \\ - \int_{L_x} \int_{L_z} \int_0^{k_t} [T_{12} - \rho \bar{u} \bar{v}] dy dz dx - \int_{L_x} \int_{L_z} \int_0^{k_t} y P_x dy dz dx . \quad (4.3)$$

Here M is the moment on the surface. Following which, zero-plane displacement $d = k_t - M/(\tau_w L_x L_z)$ is calculated. With the operation $(L_x L_z)^{-1} \int_{L_x} \int_{L_z} [T_{12} - \rho \bar{u} \bar{v}] dz dx$ dispersive stress is included in the total shear stress and is labeled as τ_{tot} (Jackson 1981). Kameda *et al.* (2018) calculated the displacement d by setting the wall coordinate origin at k_t , thus the equation for the zero-plane displacement d writes:

$$d = k_t - \frac{\int_0^{k_t} (\tau_{tot} + y P_x) dy}{\tau_w} . \quad (4.4)$$

REFERENCES

- AGHAEI JOUYBARI, M., YUAN, J., BRERETON, G. J. & MURILLO, M. S. 2021 Data-driven prediction of the equivalent sand-grain height in rough-wall turbulent flows. *Journal of Fluid Mechanics* **912**, A8.
- ALVES PORTELA, F. & SANDHAM, N.D. 2020 A DNS/URANS approach for simulating rough-wall turbulent flows. *International Journal of Heat and Fluid Flow* **85**, 108627.
- ANDERSON, W. & MENEVEAU, C. 2011 Dynamic roughness model for large-eddy simulation of turbulent flow over multiscale, fractal-like rough surfaces. *Journal of Fluid Mechanics* **679**, 288–314.
- BARROS, J. M. & CHRISTENSEN, K. T. 2019 Characteristics of large-scale and superstructure motions in a turbulent boundary layer overlying complex roughness. *Journal of Turbulence* **20** (2), 147–173.
- BARROS, J. M., SCHULTZ, M. P. & FLACK, K. A. 2018 Measurements of skin-friction of systematically generated surface roughness. *International Journal of Heat and Fluid Flow* **72**, 1 – 7.
- BHAGANAGAR, K. 2008 Direct numerical simulation of unsteady flow in channel with rough walls. *Physics of Fluids* **20** (10), 101508.
- BONS, J. 2005 A critical assessment of reynolds analogy for turbine flows. *Journal of Heat Transfer* **127** (5), 472–485.
- BONS, J. P., TAYLOR, R. P., MCCLAIN, S. T. & RIVIR, R. B. 2001 The many faces of turbine surface roughness. *Journal of Turbomechanics* **123**, 739–748.
- BUSSE, A., LÜTZNER, M. & SANDHAM, N. D. 2015 Direct numerical simulation of turbulent flow over a rough surface based on a surface scan. *Computers & Fluids* **116**, 129 – 147.
- BUSSE, A., THAKKAR, M. & SANDHAM, N. D. 2017 Reynolds-number dependence of the near-wall flow over irregular rough surfaces. *Journal of Fluid Mechanics* **810**, 196–224.
- CARDILLO, J., CHEN, Y., ARAYA, G., NEWMAN, J., JANSEN, K. & CASTILLO, L. 2013 DNS of a turbulent boundary layer with surface roughness. *Journal of Fluid Mechanics* **729**, 603–637.
- CHAN, L., MACDONALD, M., CHUNG, D., HUTCHINS, N. & OOI, A. 2015 A systematic investigation of roughness height and wavelength in turbulent pipe flow in the transitionally rough regime. *Journal of Fluid Mechanics* **771**, 743–777.
- CHAN, L., MACDONALD, M., CHUNG, D., HUTCHINS, N. & OOI, A. 2018 Secondary motion in turbulent pipe flow with three-dimensional roughness. *Journal of Fluid Mechanics* **854**, 5–33.
- CHAN-BRAUN, C., GARCÍA-VILLALBA, M. & UHLMANN, M. 2011 Force and torque acting on particles in a transitionally rough open-channel flow. *Journal of Fluid Mechanics* **684**, 441–474.
- CHAU, L. & BHAGANAGAR, K. 2012 Understanding turbulent flow over ripple-shaped random roughness in a channel. *Physics of Fluids* **24** (11), 115102.
- CHEVALIER, M., SCHLATTER, P., LUNDBLADH, A & HENNINGSON, D. 2007 SIMSON—A pseudo-spectral solver for incompressible boundary layer flow. *Tech. Rep. TRITA-MEK 2007:07, Royal Institute of Technology, Stockholm, Sweden* pp. 1–100.
- CHUNG, D., CHAN, L., MACDONALD, M., HUTCHINS, N. & OOI, A. 2015 A fast direct numerical simulation method for characterising hydraulic roughness. *Journal of Fluid Mechanics* **773**, 418–431.
- CHUNG, D., HUTCHINS, N., SCHULTZ, M. P. & FLACK, K. A. 2021 Predicting the drag of rough surfaces. *Annual Review of Fluid Mechanics* **53**, 439–471.
- CLAUSER, F. H. 1956 The turbulent boundary layer. *Advances in Applied Mechanics*, vol. 4, pp. 1 – 51.
- COCEAL, O. & BELCHER, S.E. 2004 A canopy model of mean winds through urban areas. *Quarterly Journal of the Royal Meteorological Society* **130** (599), 1349–1372.
- DE MARCHIS, M, SACCONI, D. & MILICI, B. 2020 Large eddy simulations of rough turbulent channel flows bounded by irregular roughness: Advances toward a universal roughness correlation. *Flow, Turbulence and Combustion* **105**, 627–648.
- FINNIGAN, J. J. & SHAW, R. H. 2008 Double-averaging methodology and its application to turbulent flow in and above vegetation canopies. *Acta Geophys.* **56** (1), 534 – 561.
- FLACK, K.A., SCHULTZ, M.P. & BARROS, J.M. 2020 Skin friction measurements of

- systematically-varied roughness: Probing the role of roughness amplitude and skewness. *Flow, Turbulence and Combustion* **104** (2-3), 317–329.
- FLACK, K., SCHULTZ, M., BARROS, J. & KIM, Y.C. 2016 Skin-friction behavior in the transitionally-rough regime. *International Journal of Heat and Fluid Flow* **61**, 21–30.
- FLACK, K. A. 2018 Moving beyond moody. *Journal of Fluid Mechanics* **842**, 1–4.
- FLACK, K. A. & SCHULTZ, M. P. 2010 Review of hydraulic roughness scales in the fully rough regime. *Journal of Fluids Engineering* **132** (4).
- FLACK, K. A., SCHULTZ, M. P. & CONNELLY, J. S. 2007 Examination of a critical roughness height for outer layer similarity. *Physics of Fluids* **19** (9), 095104.
- FLORES, O. & JIMÉNEZ, J. 2010 Hierarchy of minimal flow units in the logarithmic layer. *Physics of Fluids* **22** (7), 071704.
- FOROOGHI, P., STRIPF, M. & FROHNAPFEL, B. 2018a A systematic study of turbulent heat transfer over rough walls. *International Journal of Heat and Mass Transfer* **127**, 1157–1168.
- FOROOGHI, P., STROH, A., MAGAGNATO, F., JAKIRLIĆ, S. & FROHNAPFEL, B. 2017 Toward a universal roughness correlation. *Journal of Fluids Engineering* **139** (12), 121201.
- FOROOGHI, P., STROH, A., SCHLATTER, P. & FROHNAPFEL, B. 2018b Direct numerical simulation of flow over dissimilar, randomly distributed roughness elements: A systematic study on the effect of surface morphology on turbulence. *Phys. Rev. Fluids* **3**, 044605.
- FOROOGHI, P., WEIDENLENER, A., MAGAGNATO, F., BÖHM, B., KUBACH, H., KOCH, T. & FROHNAPFEL, B. 2018c DNS of momentum and heat transfer over rough surfaces based on realistic combustion chamber deposit geometries. *International Journal of Heat and Fluid Flow* **69**, 83 – 94.
- GOLDSTEIN, D., HANDLER, R. & SIROVICH, L. 1993 Modeling a no-slip flow boundary with an external force field. *Journal of Computational Physics* **105** (2), 354–366.
- HAMA, F.R., OF NAVAL ARCHITECTS, SOCIETY & ENGINEERS, MARINE 1954 *Boundary-layer Characteristics for Smooth and Rough Surfaces*, by Francis R. Hama.
- HUTCHINS, N., MONTY, J.P., NUGROHO, B., GANAPATHISUBRAMANI, B. & UTAMA, IKAP 2016 Turbulent boundary layers developing over rough surfaces: from the laboratory to full-scale systems. In *20th Australasian fluid mechanics conference*, , vol. 1235.
- JACKSON, P. S. 1981 On the displacement height in the logarithmic velocity profile. *Journal of Fluid Mechanics* **111**, 15–25.
- JELLY, T. O. & BUSSE, A. 2018 Reynolds and dispersive shear stress contributions above highly skewed roughness. *Journal of Fluid Mechanics* **852**, 710–724.
- JELLY, T. O. & BUSSE, A. 2019 Reynolds number dependence of reynolds and dispersive stresses in turbulent channel flow past irregular near-gaussian roughness. *International Journal of Heat and Fluid Flow* **80**, 108485.
- JIMÉNEZ, J. & MOIN, P. 1991 The minimal flow unit in near-wall turbulence. *Journal of Fluid Mechanics* **225**, 213–240.
- KAMEDA, TAKATSUGU, MOCHIZUKI, SHINSUKE & OSAKA, HIDEO 2018 On the virtual origin determined from momentum equation analysis using experimental data within the roughness sublayer. *Experiments in Fluids* **59** (10), 146.
- KUWATA, Y. & KAWAGUCHI, Y. 2019 Direct numerical simulation of turbulence over systematically varied irregular rough surfaces. *Journal of Fluid Mechanics* **862**, 781–815.
- LANGELANDSVIK, L. I., KUNKEL, G. J. & SMITS, A. J. 2008 Flow in a commercial steel pipe. *Journal of Fluid Mechanics* **595**, 323–339.
- LEONARDI, S. & CASTRO, IAN P. 2010 Channel flow over large cube roughness: a direct numerical simulation study. *Journal of Fluid Mechanics* **651**, 519–539.
- MACDONALD, M., CHUNG, D., HUTCHINS, N., CHAN, L., OOI, A. & GARCÍA-MAYORAL, A. 2016 The minimal channel: a fast and direct method for characterising roughness. *Journal of Physics: Conference Series* **708**, 012010.
- MACDONALD, M., CHUNG, D., HUTCHINS, N., CHAN, L., OOI, A. & GARCIA-MAYORAL, R. 2017 The minimal-span channel for rough-wall turbulent flows. *Journal of Fluid Mechanics* **816**, 5–42.
- MACDONALD, M., HUTCHINS, N. & CHUNG, D. 2019 Roughness effects in turbulent forced convection. *Journal of Fluid Mechanics* **861**, 138–162.
- MACDONALD, M., OOI, A., GARCÍA-MAYORAL, R., HUTCHINS, N. & CHUNG, D. 2018

- Direct numerical simulation of high aspect ratio spanwise-aligned bars. *Journal of Fluid Mechanics* **843**, 126–155.
- MACDONALD, R.W. 2000 Modelling the mean velocity profile in the urban canopy layer. *Boundary-Layer Meteorology* **97** (1), 25–45.
- MAZZUOLI, M. & UHLMANN, M. 2017 Direct numerical simulation of open-channel flow over a fully rough wall at moderate relative submergence. *Journal of Fluid Mechanics* **824**, 722–765.
- MONTY, J. P., DOGAN, E., HANSON, R., SCARDINO, A. J., GANAPATHISUBRAMANI, B. & HUTCHINS, N. 2016 An assessment of the ship drag penalty arising from light calcareous tubeworm fouling. *Biofouling* **32** (4), 451–464.
- MOODY, L.F. 1944 Friction factors for pipe flow. *Trans. ASME* **66** (8), 671–677.
- NAPOLI, E., ARMENIO, V. & DE MARCHIS, M. 2008 The effect of the slope of irregularly distributed roughness elements on turbulent wall-bounded flows. *Journal of Fluid Mechanics* **613**, 385–394.
- NIKORA, V. I., STOESSERT, T., CAMERON, S. M., STEWART, M., PAPADOPOULOS, K., OURO, P., MCSHERRY, R., ZAMPIRON, A., MARUSIC, I., FALCONER, R. A. & ET AL. 2019 Friction factor decomposition for rough-wall flows: theoretical background and application to open-channel flows. *Journal of Fluid Mechanics* **872**, 626–664.
- NIKURADSE, J. 1933 *Stroemungsgesetze in rauhen Rohren*. Berlin: VDI-Verl.
- ORLANDI, P. & LEONARDI, S. 2006 DNS of turbulent channel flows with two- and three-dimensional roughness. *Journal of Turbulence* **7**, N73.
- PERRY, A. E. & JOUBERT, P. N. 1963 Rough-wall boundary layers in adverse pressure gradients. *Journal of Fluid Mechanics* **17** (2), 193–211.
- PERRY, A. E., SCHOFIELD, W. H. & JOUBERT, P. N. 1969 Rough wall turbulent boundary layers. *Journal of Fluid Mechanics* **37** (2), 383–413.
- PLACIDI, M. & GANAPATHISUBRAMANI, B. 2015 Effects of frontal and plan solidities on aerodynamic parameters and the roughness sublayer in turbulent boundary layers. *Journal of Fluid Mechanics* **782**, 541–566.
- POPE, S. B. 2000 *Turbulent Flows*. Cambridge University Press.
- PÉREZ-RÀFOLS, F. & ALMQVIST, A. 2019 Generating randomly rough surfaces with given height probability distribution and power spectrum. *Tribology International* **131**, 591 – 604.
- QUADRIO, M. & LUCHINI, P. 2003 Integral space–time scales in turbulent wall flows. *Physics of Fluids* **15** (8), 2219–2227.
- VAN RIJ, J. A., BELNAP, B. J. & LIGRANI, P. M. 2002 Analysis and Experiments on Three-Dimensional, Irregular Surface Roughness . *Journal of Fluids Engineering* **124** (3), 671–677.
- SCHLICHTING, H. 1936 *Experimentelle untersuchungen zum rauhigkeitsproblem*. *INGENIEUR-ARCHIV* .
- SCHULTZ, M. P. & FLACK, K. A. 2009 Turbulent boundary layers on a systematically varied rough wall. *Physics of Fluids* **21** (1), 015104.
- SCOTTI, A. 2006 Direct numerical simulation of turbulent channel flows with boundary roughened with virtual sandpaper. *Physics of Fluids* **18** (3), 031701.
- SIGAL, A. & DANBERG, JAMES E. 1990 New correlation of roughness density effect on the turbulent boundary layer. *AIAA Journal* **28** (3), 554–556.
- STROH, A., SCHÄFER, K., FROHNAPFEL, B. & FOROOGHI, P. 2020 Rearrangement of secondary flow over spanwise heterogeneous roughness. *Journal of Fluid Mechanics* **885**, R5.
- THAKKAR, M., BUSSE, A. & SANDHAM, N. 2017 Surface correlations of hydrodynamic drag for transitionally rough engineering surfaces. *Journal of Turbulence* **18** (2), 138–169.
- TOWNSEND, A. A. 1976 *The structure of turbulent shear flow* / A.A.Townsend, 2nd edn. Cambridge University Press Cambridge [Eng.] ; New York.
- VANDERWEL, C., STROH, A., KRIEGSEIS, J., FROHNAPFEL, B. & GANAPATHISUBRAMANI, B. 2019 The instantaneous structure of secondary flows in turbulent boundary layers. *Journal of Fluid Mechanics* **862**, 845–870.
- VELANDIA, J. & BANSMER, S. 2019 Topographic study of the ice accretion roughness on a generic aero-engine intake.
- WAIGH, D.R. & KIND, R.J. 1998 Improved aerodynamic characterization of regular three-dimensional roughness. *AIAA journal* **36** (6), 1117–1119.

- YANG, X. I. A., SADIQUE, J., MITTAL, R. & MENEVEAU, C. 2016 Exponential roughness layer and analytical model for turbulent boundary layer flow over rectangular-prism roughness elements. *Journal of Fluid Mechanics* **789**, 127–165.
- YUAN, J. & AGHAEI JOUYBARI, M. 2018 Topographical effects of roughness on turbulence statistics in roughness sublayer. *Phys. Rev. Fluids* **3**, 114603.
- YUAN, J. & PIOMELLI, U. 2014 Estimation and prediction of the roughness function on realistic surfaces. *Journal of Turbulence* **15** (6), 350–365.